

MSc Biomedical Engineering

Fatigue Testing of 3D-Printed Compliant Joints: An Experimental Study

Masters Thesis

Lauren Safai 4613937

Delft University of Technology

Supervisors :

Prof.dr.ir A.A. Zadpoor
Dr.ir G. Smit
Ir. J.S Cuellar



Challenge the future

Fatigue Testing of 3D-Printed Compliant Joints: An Experimental Study

By
Lauren Safai
4613937

in partial fulfillment of the requirements for the degree of

Master of Science
in Biomedical Engineering

at the Delft University of Technology
to be defended publicly on Friday, October 19, 2018, at 11:00 AM

Supervisors: Prof.Dr.Ir A.A. Zadpoor
 Dr.Ir G. Smit
 Ir. J.S. Cuellar

Biomaterials and Tissue Biomechanics Specialization
Biomechanical Engineering Department
Faculty of Mechanical, Maritime, and Materials Engineering
Delft University of Technology

Abstract

As interest in additive manufacturing, or 3D printing, increases, technological improvements are making printing methods quicker and more cost efficient. Inventors and innovators are able to print low-cost and complex geometries rapidly as a result of the manufacturing time being reduced from weeks to hours. With the large amount of polymeric materials available, the design and manufacturing of products are continuously changing as more industries adopt the use of additive manufacturing. One up-and-coming application of additive manufacturing is monolithic compliant joints, which use the elastic deformation of the flexural arms as a mechanism for to complete the desired function. With additive manufacturing becoming more prevalent, it is essential that parts are able to withstand the mechanical and environmental stresses that occur during use. Understanding a material's response to cyclic loading and unloading is important, as the majority of parts will experience fatigue behavior. Fatigue is a progressive and permanent structural change that could result in a crack or complete rupture, making a part unable to perform its desired task. Since additive manufacturing of compliant joints is a new field, it is critical to understand fatigue behavior in 3D-printed parts so that fatigue behavior can be predicted and prevented.

Acknowledgements

I would like to thank my daily supervisors, Juan Cuellar and Gerwin Smit, who provided this opportunity for me and guided me throughout the entire thesis. They were involved in all aspects of my project from the literature review to the colloquia and to the thesis. As well, thank you to Amir Zadpoor for providing feedback and guidance when it was needed.

To my friends, Niko Putra, Kate Loe, and Arjen Jongschaap, thank you so much for listening to all of my ideas and talking them through with me whenever I needed. My project only became that much better through discussing with you. Finally, I would like to thank my family for their unwavering support and encouragement throughout my entire degree.

The cover photograph of a bee wing was taken by John Cromwell*.

Table of Contents

1. Introduction	6
1.1 Compliant Joints	6
1.1.1 <i>General</i>	6
1.1.2 <i>Design</i>	7
1.1.3 <i>Applications</i>	8
1.2 Designing Complaint Joints	8
1.2.1 <i>Classification</i>	8
1.2.2 <i>Fabrication</i>	8
1.2.3 <i>Evaluation</i>	9
1.3 Fatigue	9
1.3.1 <i>Fatigue in Polymers</i>	9
1.3.2 <i>Factors affecting 3D-printed polymers</i>	9
1.3.3 <i>Standardization</i>	10
1.4 Problem Statement	10
1.5 Thesis Aim	11
2. Methods	12
2.1 Design Constraints	12
2.1.1 <i>Degrees of Freedom</i>	12
2.1.2 <i>Range of Motion</i>	12
2.1.3 <i>Size</i>	13
2.2 Printer Selection	14
2.3 Material Selection	14
2.4 Joint Selection	16
2.4.1 <i>Cross Axis Hinge</i>	16
2.4.2 <i>Contact Bearing</i>	21
2.4.3 <i>Spiral</i>	26
2.4.4 <i>Final Designs</i>	31
2.5 Printing Parameters	32
2.6 Testing Setup	33
2.6.1 <i>Clamping Stand</i>	33
2.6.2 <i>Instron Settings</i>	34
2.7 Testing	35
3 Results	36
3.1 First Test Iteration	36
3.2 Second Test Iteration	36
3.3 Third Test Iteration	37
3.1.1 <i>Cross Axis Hinge</i>	37
3.1.2 <i>Spiral</i>	40
4 Discussion	43
4.1 Analytical and Numerical Model Comparison	43
4.2 Material Behavior	43
4.3 Geometry Behavior	44
4.4 Limitations	45
4.5 Literature Comparison	46
4.6 Future Work	46
5 Conclusion	48

6	References	49
7	Appendix	56
A	Initial Matlab Codes	56
B	Technical Drawings	59
C	First Iteration Pictures	60
D	Second Iteration Pictures	61
E	Cross Axis Hinge Abaqus Stress Distribution	64
F	Cross Axis Hinge Fatigue Result Pictures	65
G	New Spiral Matlab Code	68
H	Spiral Abaqus Stress Distribution	70
I	Spiral Fatigue Result Pictures	71

1 Introduction

With the expanding interest from industry and research communities, the application of additive manufacturing (AM), or 3D printing, has been increasing [1]. Through the improvement of manufacturing technology, high-grade prints are able to be produced expeditiously and cost effectively. As a result of the greater number of polymer materials available, the design and fabrication of products are continually changing with technological advancements and consumer use [1]. Inventors and innovators are now capable of producing low-cost prototypes and complex geometries rapidly and efficiently due to the reduction in manufacturing time from weeks to hours [2]. Additive manufacturing is now found in various industries such as medicine [3-10], aerospace [11], apparel [12, 13], dentistry [14], automotive [15], electronics [2, 16], and oceanography [17], since this technique is suitable and adaptable to many applications.

Of the multiple uses of additive manufacturing, one emerging application is the fabrication of monolithic compliant joints, which use the flexibility of the joint itself to complete the desired task [18]. It is of utmost importance that, as the usage of additive manufacturing continues growing, parts are able to resist both mechanical and environmental stresses that occur during operation. It is critical to identify the required strengths for any engineering material in certain loading applications under varying conditions [19, 20]. The understanding of a material's resistance to repetitive loading and unloading is essential since most materials will probably experience fatigue [21]. The cyclic stresses and strains placed on a part in use result in fatigue, which is a progressive and permanent structural change that may end in a crack or complete rupture after a certain number of cycles. Polymers are susceptible to fatigue at applied stresses below yield or fracture stress; this may cause micro cracks in the material leading to catastrophic failure [22]. Understanding the fatigue behavior of parts fabricated with AM is critical for predicting and preventing fatigue failure.

1.1 Compliant Joints

1.1.1 General

Rather than using rigid-body joints, compliant joints transfer motion, energy, or force using elastic deformation of their flexure links (Figure 1) [23].

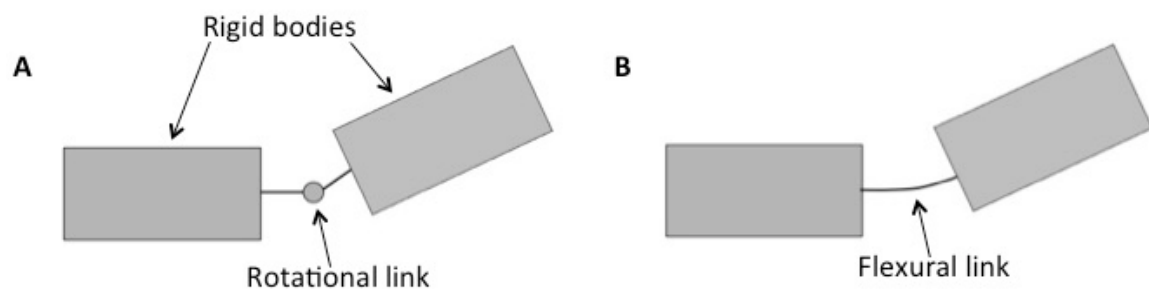


Figure 1. In a traditional rigid body linkage, A) rigid bodies are connected through conventional links that are typically comprised of multiple bodies, while in compliant joints, B) rigid bodies are connected through monolithic, flexible links.

The motion of the flexure arms comes from inputted mechanical, electrical, thermal, or magnetic energy and then transferring it into an output motion (Figure 2).

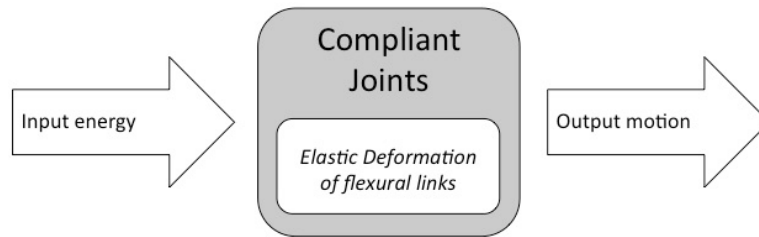


Figure 2. Here is a schematic representation of how compliant joints use an input energy to create an output motion.

Typically with traditional rigid-body joints, there is almost zero stiffness around the axis of rotation and large stiffness in the other two directions [23]. As a result of the compliancy of in compliant joints, the inherent internal stiffness makes it challenging to achieve the stiffness of a traditional rigid-body joint when fabricating a monolithic design [23]. There are numerous benefits to compliant joints, but among the most notable are no friction losses, no lubrication, compactness, ease of fabrication, weight reduction, and almost no maintenance [24, 18]. Since the compliant joints can be fabricated as monolithic structures, the required number of parts to build the mechanism is substantially reduced [18]. The reduction of moving parts in the joints also reduces the amount of wear produced; the joint's overall precision is improved since the backlash is substantially reduced or eliminated [18, 24, 25].

Despite all of the benefits, several drawbacks or challenges associated with compliant joints still need to be addressed. When integrating multiple functions into a fewer number of parts, the design requires the simultaneous analysis of motion and force behavior, where the motion is typically in the nonlinear range [18]. Additionally, the rotation of the compliant joints is not pure because the deformation of the flexural joints is a result of axial shearing and torsion loading in addition to bending [24]. During deflection, the center of rotation is not fixed and displaces under loading [24]. Finally, because the rigid-body parts have been removed from the design, the failure of the compliant joint will likely be a result of fatigue or overloading [24]. Since the motion is a result of bending, the flexural parts will experience stress at these locations. Due to the repeated loading of the flexural arms, fatigue loads will be present in the design [18]. The fatigue life is a critical factor for compliant joints since the fatigue life must exceed the expected life of the compliant joint in order to be able to perform the given function [18].

1.1.2 Design

There are two methods that have been used to design compliant joints: the rigid-body-replacement method and the freedom and constrain topologies method (FACT). In the rigid-body-replacement method, the initial step is to find rigid-body mechanisms that are able to accomplish the desired function. Next, a pseudo-rigid-body model is created and subsequently converted into a compliant joint by replacing rigid-body parts with compliant structures [26-30]. In this method, torsion springs are used to represent compliant joints [18, 23]. Using a different approach, the FACT method takes the desired motion of the compliant joint and converts that into the needed

degrees of freedom. From the degrees of freedom, geometric entities are found that are able to perform the desired motion. With these geometric entities, a possible topology is generated to recreate the motion within the constraint space.

1.1.3 Applications

Compliant joints have been incorporated into the design and manufacturing of multitude of industries, such as electronics, outdoor wear, medical devices, home goods, packaging, aerospace, automotive, and construction, for both high-end, high-precision devices or ultralow-cost packing [18, 24]. The applications include robotic micro-displacement mechanisms, high-precision cameras, missile-control devices, piezoelectric actuators and motors, orthotic prostheses, nano-imprint technology, nanoscale bioengineering, or valves [18, 24].

1.2 Designing Compliant Joints

1.2.1 Classification

Compliant joints are classified based on the kinematic degrees of freedom in the joint [23]. There are revolute, translational, universal, and spherical joints. Revolute compliant joints are designed to have only pure rotational motions around one axis, while translational joints are designed to allow one degree of freedom along one axis. These two joints have the most basic motions since they are designed for one degree of freedom. A more complex design, the universal compliant joint, allows for two rotational degrees of freedom. Finally, the most complicated joint is the spherical joint that allows for three degrees of rotational freedom, as does its' translational mechanical counterpart.

Compliant joints may also be classified at primitive flexure joints or complex flexure joints, which is a combination of two or more primitive flexure joints [31]. Within the primitive flexure joints, there are also small-length flexure pivots and long-length segments [32]. Notch type joints are considered small-length flexure pivots; curve-beam, leaf spring, tape spring, and contact-based flexures are considered long-length segments.

1.2.2 Fabrication

Compliant joints can be fabricated with various techniques depending on the scale of the part and the material used. Different fabrication techniques include precision milling [33], EDM [34, 35], laser cutting [36], molding [37], and additive manufacturing [38-40].

Even though conventional manufacturing techniques are still employed, their usage is often limited to simple mechanisms. With more advanced designs, more complex assembly procedures are required to construct compliant joints. Since compliant joints are monolithic structures, the development of one-step fabrication techniques is key since there is no need for post-manufacturing assembly. In this instance, additive manufacturing is the most feasible solution because it has the ability to create continuous, complex 3D structures without the need for specialized manufacturing skills or demanding labor procedures [41].

1.2.3 Evaluation

When comparing compliant joints, there are several criteria that may be used to evaluate and compare the joints. The first measure, range of motion, is defined as the motion between the deflection limits that does cause material failure. Material failure occurs when the stress exceeds the yield stress, and elastic deformation becomes plastic deformation. A second measure is axis drift; it is motion of the center of rotation from its original position or the deviation from straight-line motion. Lastly, the ratio of off-axis stiffness to on-axis stiffness is defined as the stiffness along the undesired axes to the stiffness along the desired axis.

1.3 Fatigue

1.3.1 Fatigue in Polymers

Fatigue, due to repetitive loading and unloading (i.e. cyclic loading) of loads less than the ultimate tensile strength and yield strength, is the progressive build-up of structural damage in a material. There are two different processes through which polymers experience fatigue failure [42, 43]: (1) thermal failure is caused by hysteretic heating causing thermal softening and melting, or (2) mechanical failure is a result of the initiation of crack that propagate through the material. In the case of thermal fatigue, hysteretic heating is caused by relatively high frequencies or strain rates as a result of high damping, viscoelasticity, and low thermal conductivity [44, 45]. The temperature of the specimen rises while the specimen stiffness decreases due to hysteretic energy being dissipated as heat. The stiffness loss causes the specimen to deflect and deform more. During mechanical failure, intrusions and extrusions (i.e. dislocations) along the material surface begin the failure process and cause surface roughening [46, 47]. The intrusions and extrusions along the surface next form slip bands, which nucleate into micro cracks or localized debonding of the material, known as crack initiation [46, 48, 49]. During the microstructure-sensitive stage, the crack gradually propagates through the microscopic obstacles of the material after initial crack nucleation or initiation, which is called crack propagation [48]. During this stage, the crack growth rate fluctuates as a result of encountering multiple grain boundaries [50, 51]. Eventually, the crack growth becomes micro structurally independent and continues to grow until the final rupture of the material [47, 48]. From the work of [52], a clear distinction is made between thermal and mechanical failure, where the first may not have a crack at the point of failure, while the latter is a physical separation process.

1.3.2 Factors affecting 3D-printed polymers

As a result of the anisotropic properties and residual stresses from layer deposition, the fatigue testing of 3D-printed specimens is challenging [20]. The mechanical characterization, including fatigue life, of parts fabricated with various 3D printing techniques are affected by different variables. For extrusion based printing, the variables that effect mechanical characterization include: layer height and bead width, build orientation, fiber orientation, and air gap between filaments [20, 53-56]. Some variables that affect powder based printing methods are layer height, build orientation, laser power, scan length, recycled powder content, crystallization temperature, and

powder bed temperature [20, 57]. In polyjetting, the parts are affected by the presence of additives, being printed on an over-cured surface, the presence of additives, the physics and chemistry of polymer fusion, and unknown manufacturer resin formulations [20]. Fatigue is problematic to predict due to the synergism between all of these variables. The microstructure of the part, such as defect type and grain size, is influenced by these variables, which, in turn, affects the part's mechanical behavior [58].

1.3.3 Standardization

There are two groups that address the standardization of mechanical testing of 3D-printed materials and specimens: the American Society of Testing and Materials (ASTM) and the International Standards Organization (ISO) [20]. There is currently a limited amount of standardizations for 3D printing, especially in terms of fatigue.

In the standard, ASTM D7791, uniaxial fatigue testing in tension or compression is addressed [59]. There is no equivalent with ISO. During testing, the sample can be cycled between 1-25 Hz, but a frequency below 5 Hz is recommended to avoid or reduce the generation of heat. The stress or strain is measured as a function of cycles, where failure limit is defined as when the specimen fails or reaches 10^7 cycles. Testing is only conducted within the elastic limit of the material. Similarly, ASTM D3479 tests tension fatigue of a polymer matrix composite material with defined loading and environmental conditions [60].

There are two standards, ASTM D7774 and ISO 13003, for flexural fatigue in plastics that both have sinusoidal loading but differ technically [61, 62]. For ASTM D7774, three or four point bending. Stress or strain cycling fluctuates between positive and negative directions, where the loads do not exceed the proportional limit and there is an R ratio of -1. Again, the fatigue limit is when the specimen fails or reaches 10^7 cycles. In the second standard, ISO 13003, ultimate tensile and flexural strength are calculated for the fatigue loading rate. In the desired range of interest for the stress or strain or the range of interest for the fatigue life, tests are performed at four fatigue levels. With strain control, the end of the test, when the sample stiffness is reduced by 20%, is defined in terms of damage level.

Finally, two standards, ASTM D6115 and ISO 15850, investigate the relationship between crack propagation (fatigue delamination) and the interlaminar region of a fiber composite [63, 64]. It is uncertain whether or not 3D-printed materials would be able to meet assumptions of these standards since they deal specifically with composites.

1.4 Problem Statement

Since additive manufacturing of compliant joints is a relatively new field of research, there has been limited investigation into the mechanical behavior of these joints, particularly in the area of fatigue. In order for compliant joints to be implemented into various applications, it is vital to comprehend and analyze how 3D printed compliant joints behave under fatigue conditions.

1.5 Thesis Aim

In order to analyze compliant joints in cyclic loading conditions, the aim of this thesis was to investigate the fatigue life properties of different compliant revolute joint geometries fabricated using varying materials. From experimental testing results, the mechanical stability of the specific designs and the material responses would be analyzed to determine the suitability of these combinations in long-term applications.

2 Methods

2.1 Design Constraints

The design constraints were based on the assumption that the compliant joint would be able to function as a one degree of freedom revolute, hinge joint in biomedical applications, such as within an orthopedic hand prosthesis. The simplest example of hinge joints in the hand are the interphalangeal joints located in the fingers and thumb (Figure 3).

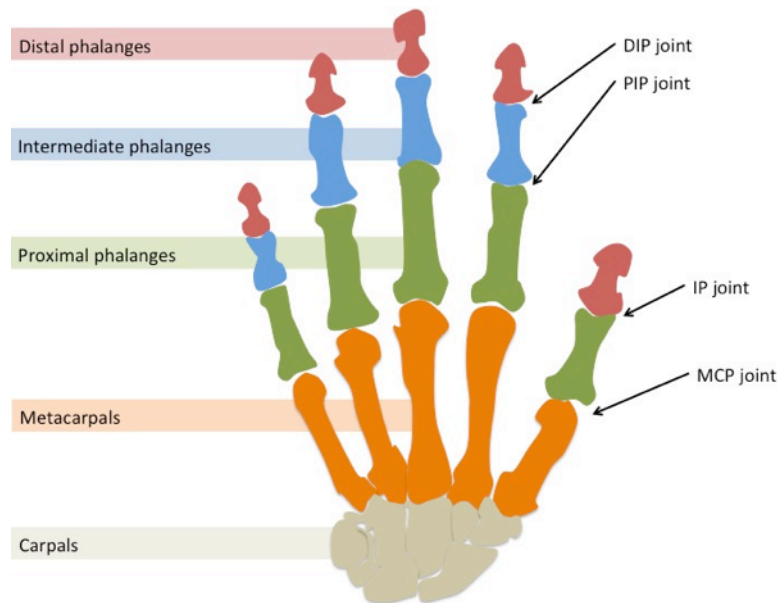


Figure 3. There are several hinge joints located throughout the hand, with two hinge joints in each finger and two in the thumb.

There are two hinge joints in each finger and in the thumb, making a total of twenty hinge joints in the hands. Within the hand, the hinge joints are the proximal interphalangeal joints (PIP) and the distal interphalangeal joints (DIP) in the fingers and the interphalangeal joint (IP) and metacarpophalangeal joints (MCP) in the thumb [65].

2.1.1 Degrees of Freedom

One of the main considerations when narrowing compliant joint designs was the degrees of freedom allowed in the joints. Focusing on the hinge joints in the hand, the compliant joint should only have one degree of rotational freedom. Therefore, the only compliant joint designs that were considered were classified as revolute joints since they did not allow translational motion.

2.1.2 Range of Motion

The range of motion for each joint varies between the different joints and fingers [65, 66]. Understanding the functional range of motion (FROM) of the hand joints compared with the active range of motion (AROM) is important since the

compliant joint design should be able to displace enough to perform daily activities. The AROM is the maximum range of motion, while the FROM is the range of motion needed to complete specific tasks or be functional. According to several studies, the functional range of motion is less than the active range of motion [65-68]. The normal range of motion in the hinge joints can be seen in Table 1 [66, 68].

	Normal ROM Fingers (Degrees)	Normal ROM Thumb (Degrees)
MCP	-	0-56
PIP	0-105	-
DIP	0-85	-
IP	-	-5-73

Table 1. The normal range of motion for the proximal interphalangeal joints, the distal interphalangeal joints (DIP), the interphalangeal joint (IP), and the metacarpophalangeal joints (MCP) are shown.

As previously stated, the FROM has a decreased range of motion compared with the AROM. In Table 2, the FROM of the different joints are listed according to Hume et al. 1990, but Pham et al. 2014 obtained similar values as well.

	FROM Fingers (Degrees)	FROM Thumb (Degrees)
MCP	-	10-32
PIP	36-86	-
DIP	20-61	-
IP	-	2-43

Table 2. The normal range of motion for the proximal interphalangeal joints, the distal interphalangeal joints (DIP), the interphalangeal joint (IP), and the metacarpophalangeal joints (MCP) are shown.

Looking at the functional range of motion, the maximum deflection angle seen is 86 degrees and the minimum is two degrees. When designing for the compliant joints, their range of motion should include the entire range of functional values. Taking this into consideration, it was chosen that the compliant joints should be able to deflect over a range of motion of zero to ninety degrees.

2.1.3 Size

In addition to both the degree of freedom and range of motion constraints, a size constraint was also implemented so that the size of the joint was relatively proportional to the size of the finger joints. Due to the variance in size of the different joints and fingers in the hand, the dimensions of the size constraint were based on the dimensions of the index finger (digit two) and middle finger (digit three).

It was found that the diameter of the index finger varies between sixteen and twenty mm [69], which also corresponds to the width, w , of the index finger (Figure 4). In a different study, specifically looking at male construction workers in India, the thickness of the middle finger increased from the distal tip to the base of the finger [70]. The average thickness in the middle finger varied from a thickness (t_1) of 12.99 mm to (t_2) 15.51 mm to (t_3) to 19.08 mm (Figure 4).

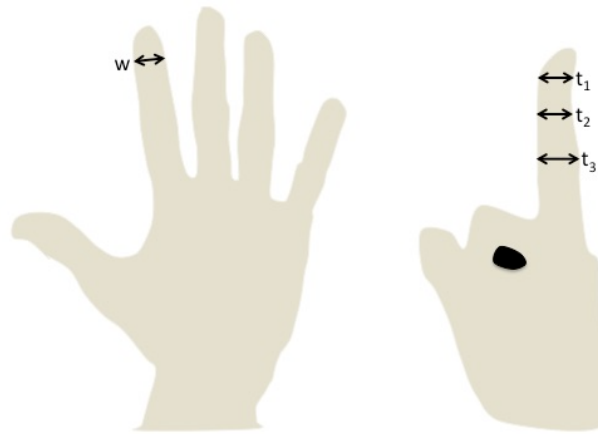


Figure 4. A) The width of the index finger, w , varies between 16 mm and 20mm [70], while B) the thickness of the middle finger varies from 12.99 mm, t_1 , to 19.08 mm, t_3 [71].

Based on the dimensions of the index and middle finger, a size constraint of $20 \times 20 \times 20 \text{ mm}^3$ was chosen, meaning that the compliant joint would have to fit within this size constraint.

2.2 Printer Selection

Given the chosen material was polymers, several types of additive manufacturing, such as selective laser melting, would not be viable options since they are specifically for metals. There are seven different methods to 3D print polymers, which are fused deposition modeling (FDM), stereolithography (SLA), digital light processing (DLP), selective laser sintering (SLS), three-dimensional printing (3DP), laminated object manufacturing (LOM), and polyjet technology [1].

Of these technologies, the only option available for printing was fused deposition modeling. The printer used was an Ultimaker 3 (Ultimaker B.V., Geldermalsen, The Netherlands) along with the Ultimaker Cura software (Ultimaker B.V., Geldermalsen, The Netherlands). The advantages of FDM technology are that it is cost-effective, has a broad range of materials, has relatively no geometry restrictions, has high print speeds, and is accessible [1]. While there are many benefits for this technology, there are also some disadvantages. Some of these include limited build size, support material usage, small dimension printing inaccuracy, and temperature fluctuations [1].

2.3 Material Selection

The available materials were a consequence of the chosen 3D printer, the Ultimaker 3 FDM printer. This printer was rated to use nine materials: nylon, polylactic acid (PLA), tough PLA, acrylonitrile butadiene styrene (ABS), copolyester (CPE), CPE+, polycarbonate, thermoplastic polyurethane (TPU) 95A, and polypropylene [72]. When designing for compliant joints, it is important that the material is both flexible and strong, since the joints use elastic deformation in order to transmit force, energy, or motion [23, 24]. To be both flexible and strong, the material should have a low young's modulus and high yield strength. According to *The Handbook of Compliant Mechanisms*, one approach for comparing different materials is to look at the ratio of yield strength to the young's modulus [18]. This parameter affects the plastic behavior of the material, where a higher ratio is better. A similar method to compare materials is to examine the resilience of the material, where the modulus of resilience is equal to

one-half the yield strength squared divided by the young's modulus [18]. The modulus of resilience is a measure of the maximum energy that can be absorbed per unit volume by the material without creating permanent distortion. The resilience and ratio of strength to young's modulus were calculated using the material properties from the Ultimaker B.V. technical data sheets when available, and the Stratasys data sheets when needed [73-81] (Table 3).

	Young's Modulus (Mpa)	Yield Strength (Mpa)	Sy/E	0.5 Sy ² /E
Nylon	579	27.8	0.048	0.667
PLA	2346.5	49.5	0.021	0.522
Tough PLA	1820	37	0.020	0.376
ABS	2030	43.6	0.021	0.468
CPE	1537.5	41.1	0.027	0.549
CPE+	1128.5	35.2	0.031	0.549
PC	1944	40	0.021	0.412
TPU 95	26	8.6	0.331	1.422
PP	220	8.7	0.040	0.172

Table 3. The calculations for the ratio of strength to young's modulus and resilience for the nine polymer materials available for the Ultimaker 3 FDM printer are shown.

From Table 3, the best two materials for both the ratio of yield strength to young's modulus and resilience were Nylon and TPU 95. On the other hand, tough PLA and PC were among the worst materials for compliant joints. From these calculations, the top choices would have been TPU 95A and Nylon ideally, but the only materials readily available for printing were Nylon, ABS, and PLA.

Since Nylon was one of the best materials for compliant joints, Nylon was chosen to be one of the two materials for testing. When comparing ABS and PLA with the calculations for the ratio of yield strength to young's modulus and resilience, both materials were better in one category than the other. From Table 3, it was unclear whether or not ABS or PLA was the best option. In order to decide, temperature was taken into consideration since that is a factor in the fatigue life in polymers. As previously mentioned, under fatigue loading polymers fail both thermally and mechanically. As seen in Table 4, ABS has a higher melting temperature compared with PLA, meaning that it has better temperature resistance. With better thermal properties for fatigue loading, ABS was the better choice when compared with PLA.

Melting Temperature	
ABS	225-245 °C
PLA	145-160 °C

Table 4. This table shows the melting temperatures for ABS and PLA.

Between the available materials, Nylon, ABS, and PLA, the two materials chosen were Nylon and ABS.

2.4 Joint Selection

The first step in deciding on the compliant joint designs was to find all of the designs that had one degree of rotational freedom and investigate whether or not it had a range of motion of ninety degrees. From the review paper by Machekposhti et al. 2016, there were a total of twenty-five designs that had one degree of rotational freedom. Of these twenty-five joints, only five joints had a total range of motion of ninety degrees (Figure 5).

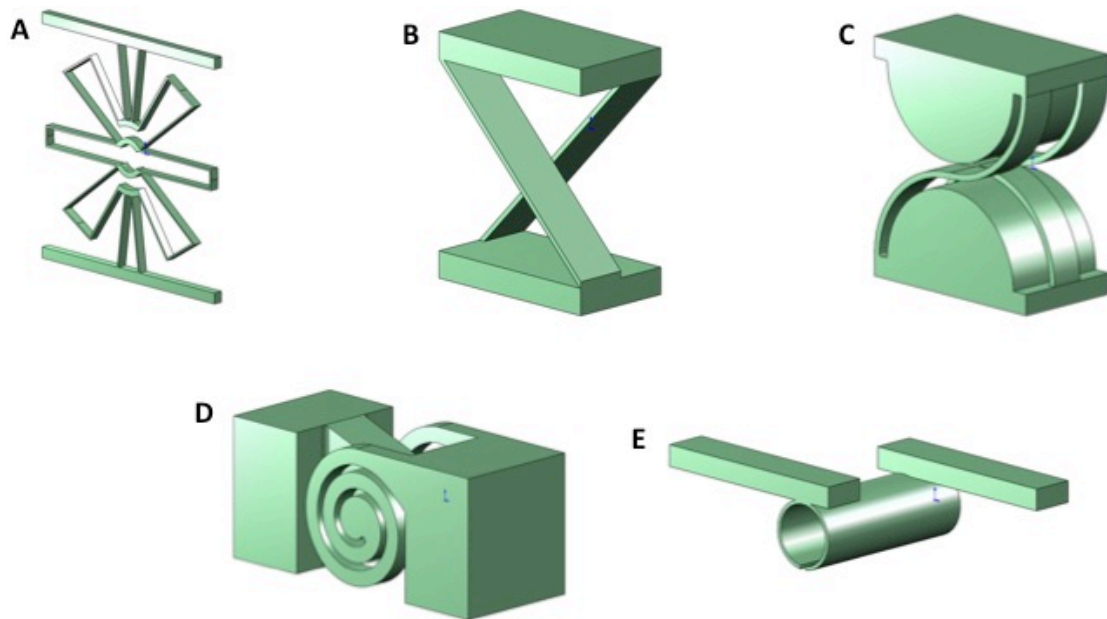


Figure 5. There were five joints, A) the flex-16, B) the cross axis hinge, C) the contact bearing, D) the spiral, and E) the split tube, that both had one degree of rotational freedom and had a range of motion of ninety degrees.

Even though each of the five joints had the needed degrees of freedom and range of motion, the flex-16 joint was eliminated because it did not fit into the size constraint. If the flex-16 design were downsized to fit the size constraint, the width of the flexures would be too small to print since the smallest dimension would be well below the 0.4 mm diameter nozzle. The remaining four joints were printed to test if they were able to reach the ninety-degree range of motion constraint. After being printed, the split tube design was unable to rotate to the ninety-degree range of motion, and broke before rotating forty-five degrees. The failure to achieve the full ninety degrees of motion was most likely due to scaling down the geometry to fit into the size constraint. As a result of the scaling, the joint was no longer able to rotate to ninety degrees, meaning that this design was no longer considered. To narrow down the three remaining designs, a stress analysis was next performed, both analytically and numerically, on the cross axis hinge, the contact bearing, and the spiral. These analyses would be used to assess if the designs, in both ABS and nylon, would experience plastic deformation when rotated to the full ninety degrees.

2.4.1 Cross Axis Hinge

In the cross axis hinge, a cantilever beam is used as the flexural-based mechanism (Figure 6). An advantage of using a cantilever beam is that it has a large range of motion because it is able to distribute stress across its geometry [81, 82]. The

maximum deflection of the cross axis hinge is dependent on the stress developed in the cantilever flexural arms [82, 83]. One factor that influences the stress in the flexural arms is the geometry of the hinge itself. The non-dimensional parameter, n , is defined as the ratio between the effective pivot length, r , and the pivot width, w (Figure 6) [83]. The variable t is defined as the flexural arm thickness and the variable l is the length of a flexural arm.

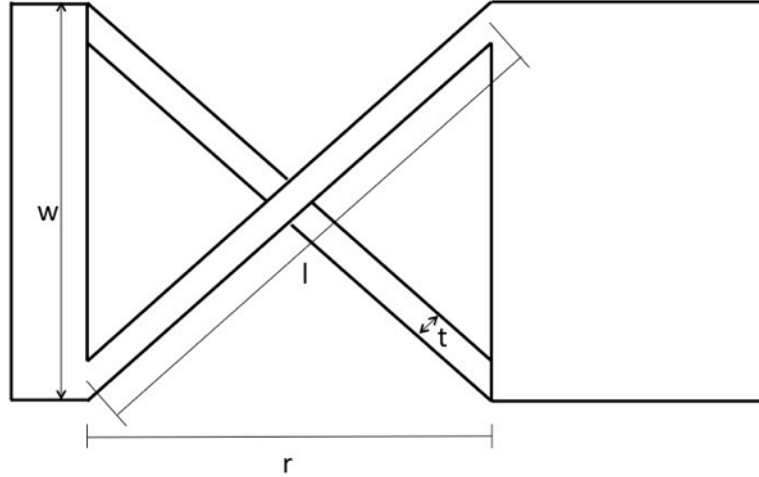


Figure 6. Here is a schematic diagram of the cross axis hinge depicting the dimensional parameters.

Using the non-dimensional parameter, n , an equation was derived by Jensen and Howell, relating the maximum stress in the flexural arms as a function of displacement [83]. In the equation, σ is the maximum stress, E is the young's modulus, and θ is the displacement angle. The relationship between stress and the deflection angle was modeled using a quadratic relationship, since a linear relationship underestimated the maximum stress:

$$\sigma = \frac{E \cdot t}{2 \cdot r} (S_1 \cdot \theta + S_2 \cdot \theta^2) \quad (1)$$

$$S_1 = 0.189394 + 0.899845 \cdot n - 0.4333 \cdot n^2 + 0.097866 \cdot n^3 - 0.00839 \cdot n^4 \quad (2)$$

$$S_2 = -0.09799 + 0.982995 \cdot n - 0.96184 \cdot n^2 + 0.413319 \cdot n^3 - 0.08387 \cdot n^4 + 0.006530 \cdot n^5 \quad (3)$$

The material parameters for ABS and Nylon (Table 5), an effective pivot length of 20 mm to fit within the size constraint, and a minimum thickness of 0.5 mm were used in the calculations. The non-dimensional parameter, n , was varied between one and four to see if there was a combination that did not experience yield stress. Through the process of trial and error, a value of one was chosen for n , since it resulted in the lowest stress values experienced by the cross axis hinge. Using these material and geometrical properties (Table 5), a plot of the stress as a function of deflection angle was calculated using MATLAB (MATLAB R2018a; The MathWorks, Inc., Massachusetts, USA) (Figure 7, Appendix A).

	ABS	Nylon
Elastic Modulus (MPa)	2030	579
Effective Pivot Length, r (mm)		20
Thickness, t (mm)		0.5
Non-dimensional Parameter, n		1

Table 5. The material and dimensional variables used for the calculations for the maximum stress in the cross axis hinge are shown.

From the plot using ABS material properties (Figure 7), the hinge is able to deflect to an angle of ninety degrees (1.5708 radians) without experiencing stresses above yield. While the hinge does not experience yield stress, the maximum stress at ninety degrees is 43.17 MPa, which is about 0.5 MPa off from the yield stress of 43.6 MPa.

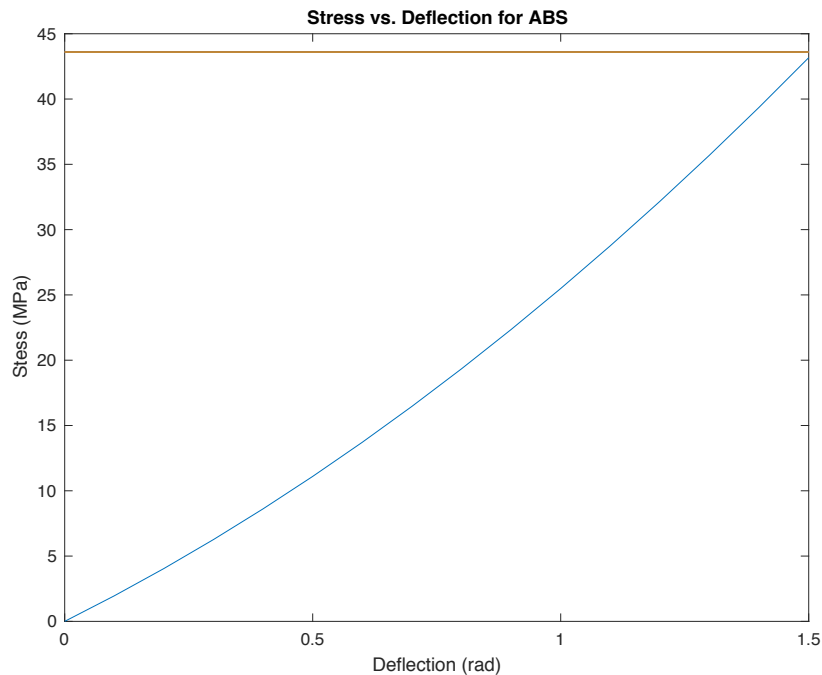


Figure 7. A plot of the deflection angle against the maximum stress in the cross axis hinge made of ABS.

In comparison with the ABS material, Nylon does not experience any stresses over the entire range of motion close to yielding (Figure 8). The maximum stress of 12.31 MPa in Nylon occurs at ninety degrees, which is substantially lower than the yield stress of 27.8 MPa.

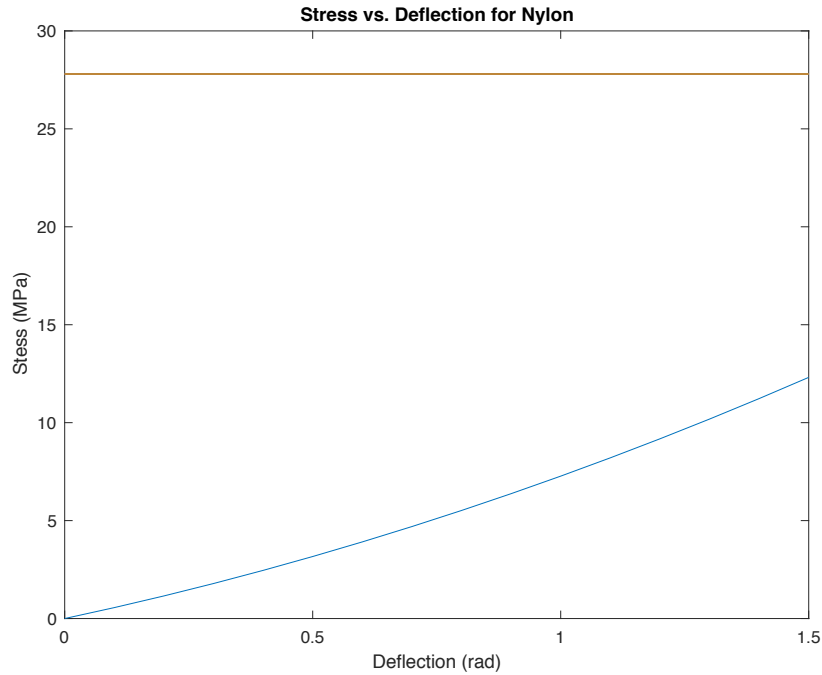


Figure 8. A plot of the deflection angle against the maximum stress in the cross axis hinge made of Nylon.

From the analytical calculations, the final design of the cross axis hinge is able to deflect across the entire range of motion for both ABS and Nylon without undergoing any plastic deformation. To verify that the analytical calculations were correct, a finite element model was created in Abqus (Abaqus 6.14; Simulia, RI, USA) to check the values numerically.

Using the final geometrical values, a solid model was created with the CAD software Solidwoks (Solidworks, Dassault Systems, Paris, France). There were three flexural arms in the model, with the outside arms having a width of two mm and the middle arm having a width of four mm, where the space between the arms was one mm [81]. With the CAD geometry, a deformable model of the cross axis hinge was developed in Abaqus. Depending on the model, two sets for material properties were used. The material properties of ABS and Nylon are listed in Table 6, where the values of the young's modulus were taken from the Ultimaker data sheet. The poisson's ratio of ABS was 0.36 [84, 85], which was experimentally found in the literature, while the poisson's ratio of Nylon was assumed to be 0.3 [86], since the exact value was unknown.

	Young's Modulus (MPa)	Poisson's Ratio
ABS	2030	0.36
Nylon	579	0.3

Table 6. The values of the young's modulus and poisson's ratio used in the finite element model for ABS and Nylon are shown.

The geometry was meshed using tetrahedral elements, where various mesh sizes were applied in order to complete a mesh convergence study. After the application of the material properties and the meshing of the geometry, boundary conditions were applied to the model. First, an encastre boundary condition was applied to one end of

the joint, preventing any rotational and translational motion (Figure 9A). Next, a reference point was created at the initial center of rotation of the joint. A kinetic coupling was then used to connect the reference point and the other joint end in order to constrain the motion of the rigid body to the motion of the reference point (Figure 9B). A displacement/rotation boundary condition was applied at the reference point, which constrained its degrees of freedom. The point was allowed to rotate ninety degrees around the axis of rotation, but it was prevented from rotating in the other two directions. As well, the point was allowed to translate in any direction.

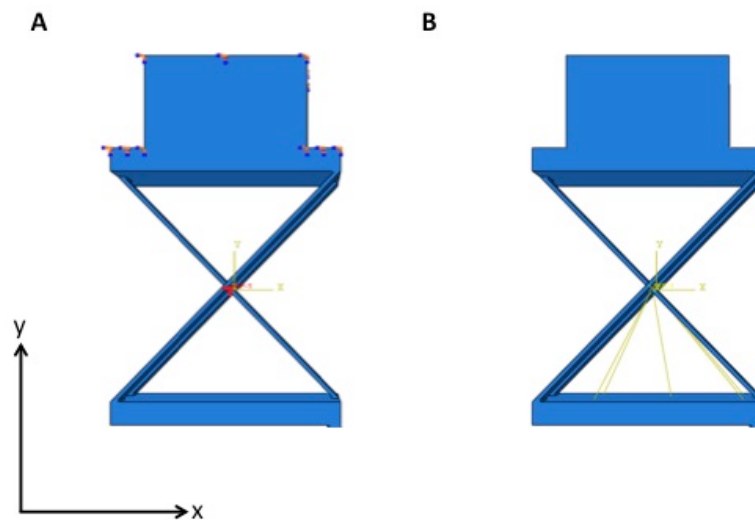


Figure 9. Two different boundary conditions were applied to the model: A) the encastre constraint prevented one end from moving, and B) the displacement/rotation condition only allowed the joint to deflect ninety degrees around the axis of rotation.

With the applications of the boundary conditions, the model was ready for simulation and the mesh convergence study. From the simulations, the maximum model stress varied between 68.18 and 43.1 MPa and 19.45 and 12.29 MPa for ABS and nylon, respectively. The global mesh seed size was varied from 1.4 mm to 0.8 mm for three simulations, which is seen in Table 7. The deformed and un-deformed states of the simulation can be seen in the figure below (Figure 10).

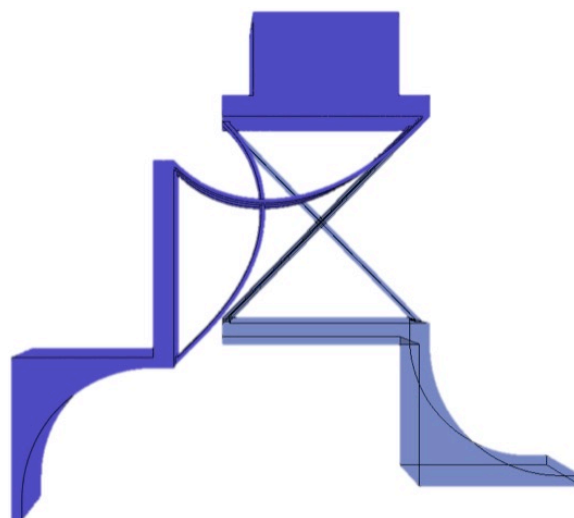


Figure 10. The un-deflected (transparent blue) and deflected (solid blue) of the cross axis hinge in the Abaqus simulations are shown.

	Global Seed Size (mm)	Maximum Stress (MPa)	Strain Energy Density (mJ/mm ³)	Analytical Stress (MPa)	Error (%)
ABS	1.4	68.18	3.33	43.17	57.93
	1.0	48.44	3.28	43.17	12.21
	0.8	43.1	3.26	43.17	0.16
Nylon	1.4	19.45	0.95	12.31	58.00
	1.0	13.6	0.94	12.31	10.48
	0.8	12.29	0.93	12.31	0.16

Table 7. The mesh convergence study for the cross axis hinge made of ABS and Nylon, where the results show that as the element size is decreased, the simulations start to converge to a solution. With the smallest mesh size, the percent error between the analytical and numerical solutions is 0.16%.

With the smallest mesh size, the cross axis hinge in ABS and nylon experienced a maximum stress of 12.29 and 43.10 MPa, respectively (Figure 11). In both cases, the maximum stress was located at the connection between the flexural arms and the base.

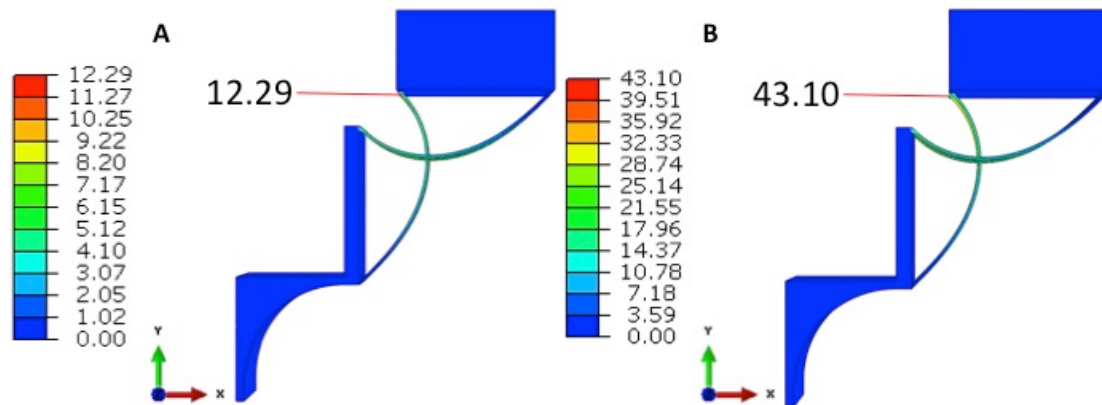


Figure 11. With a deflection of ninety degrees, the cross axis hinge has a maximum von Mises stress of A) 12.29 MPa in nylon and B) 43.10 MPa in ABS.

As can be seen from Table 7, as the size of the elements decreased, the mesh started to converge to a solution, which can be seen from the decreasing strain energy density values. The error between the analytical stress and numerical stress also decreased as the mesh size decreased. With the smallest mesh size, the percent error, for both ABS and Nylon, was 0.16%. With the verification of the calculated stress between the analytical and numerical models, this design could be used for testing.

2.4.2 Contact Bearing

The contact bearing is a rolling-contact joint design with two main components: the flexural arms and the contact, or rolling, surfaces. The flexural arms are designed to sit in between the two contact surfaces, so that when they touch one another, the arms are able to deflect without slipping (Figure 12) [87]. An advantage of this design is that the contact between the arms and rolling surfaces is able to divert compressive stresses away from the flexural arms, which are susceptible to buckling [88]. Similar to the cross axis hinge, there are three flexural arms with a width of four mm, and spacing of one mm.

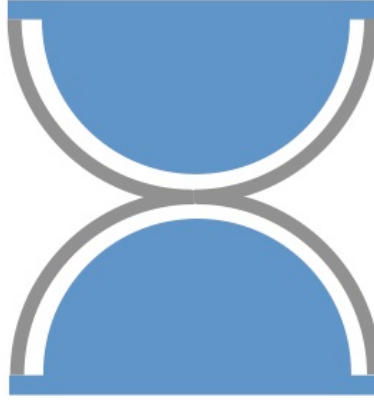


Figure 12. A diagram of the contact bearing that shows the flexible arms in grey and the contact surfaces in blue.

In order to find the maximum stress in the flexural arms, the relationship between the internal moment and curvature of the beam is first defined using the Bernoulli-Euler equation [88]:

$$M = E \cdot I \cdot \frac{d\theta}{ds} \quad (4)$$

where E is the elastic modulus, I is the moment of inertia of the cross section, and $d\theta/ds$ is the change of angle of the beam, θ , per unit of arc length, s . When the Bernoulli-Euler equation is defined in this manner, it is valid for large deflections. There were several assumptions made: 1) the material is linear elastic, 2) the shear component of deflection is small compared to shear due to bending, and 3) the beams are thin, meaning that the centroidal and neutral axes are assumed to be coincident.

The effective radius of curvature, R' , is equal to

$$R' = \frac{1}{d\theta/ds} \quad (5)$$

The effective radius of curvature also takes into account the initial curvature of the flexural arms in the undeflected state of the beam using the equation

$$R' = \left(\frac{1}{R_s} - \frac{1}{R_0} \right)^{-1} \quad (6)$$

with R_s being the radius of curvature of the surface constraining the flexural arm and R_0 being the flexural arm's initial radius of curvature (Figure 13).

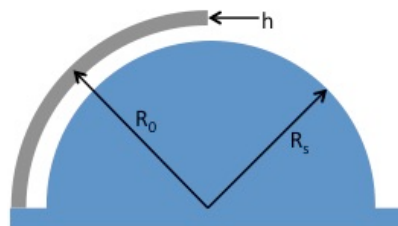


Figure 13. A diagram of half the contact bearing that shows the dimensional variables.

One assumption that is made is that the thickness of the flexural arm is small compared with R_s . If the flexural arm was initially straight, then

$$R' = R_s \quad (7)$$

Substituting equation 7 into equation 4 results in

$$M = \frac{E \cdot I}{R'} \quad (8)$$

This equation predicts that a flexural arm with a constant radius of curvature will create a moment that is also constant across the length of the flexural arm. The maximum stress through a rectangular cross section in the flexural arm is equal to

$$\sigma_{\max} = \frac{M \cdot h}{2 \cdot I} \quad (9)$$

where h is the thickness of the flexural arm. Since the moment across the flexural arm is constant, the stress should also be constant along the flexural arm. The stress is given by the equation

$$\sigma_{\max} = \frac{E \cdot h}{2 \cdot R'} \quad (10)$$

The equation predicts that the maximum stress only depends on the material, the thickness of the flexures, and the effective radius of curvature [87, 88]. Using the material properties of both Nylon and ABS previously mentioned, a plot was made for the maximum stress as a function of the radius of curvature of the contact surface using MATLAB (Appendix A). The radius of curvature for the constraining surface was varied between a minimum of one mm and a maximum of ten mm, so that the joint remained within the limits of the size constraint.

From the analytical calculations, both ABS and Nylon had values for the radius of curvature under the maximum of 10 mm that did not experience yield stress in the flexural arms (Figures 14 and 15). For ABS the minimum radius of curvature was 4.32 mm, while for Nylon the minimum radius of curvature was 2.76 mm. In order for the contact bearing to remain within the size constraint limits, the radius of curvature was chosen to be 8.25 mm.

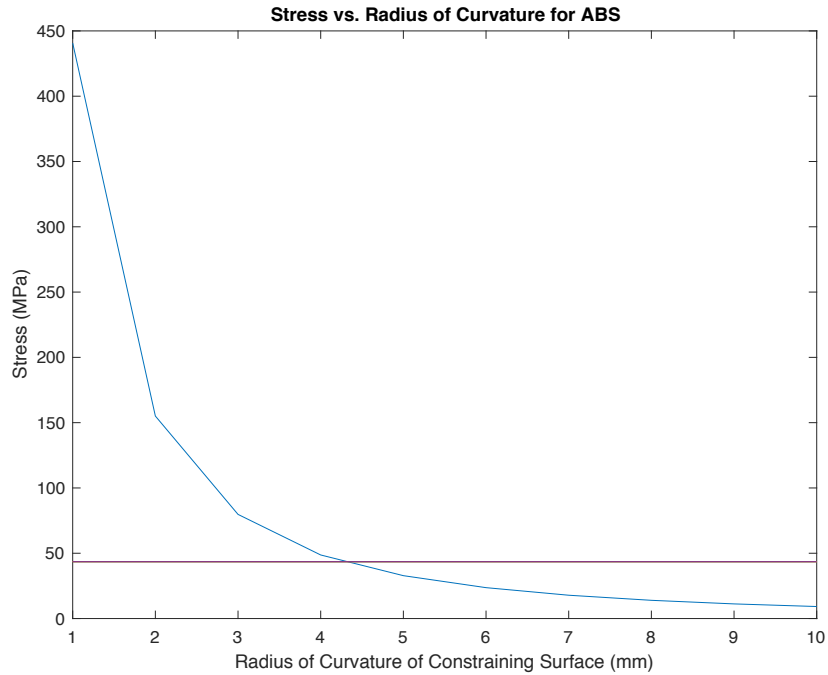


Figure 14. A plot of the radius of curvature of the contact surface against the maximum stress in the contact bearing made of ABS.

At a radius of 8.25, the maximum stress experience by ABS and Nylon is 13.3 MPa and 3.78 MPa, respectively. Both of these values are well below their respective yield stresses.

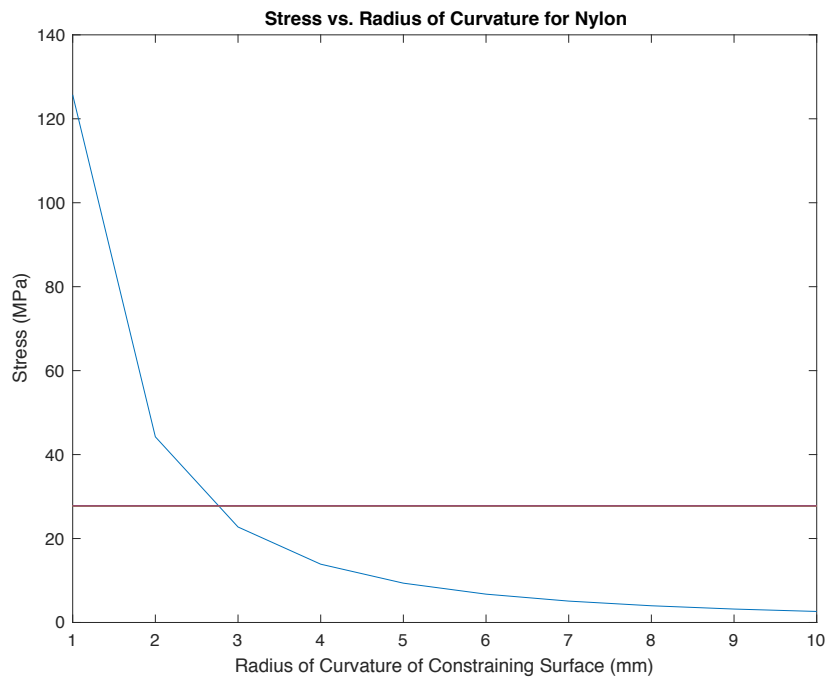


Figure 15. A plot of the radius of curvature of the contact surface against the maximum stress in the contact bearing made of Nylon

Similarly to the cross axis hinge design, the analytical calculations showed that the contact bearing, in both ABS and Nylon, should not experience yield stress during

large deflections. To check these values, a finite element model was created for the contact bearing. The model was set up in the same way as it was for the cross axis hinge, where the material properties and boundary conditions were identical. As with the cross axis hinge, a mesh convergence study was also performed. The un-deformed and deformed states of the contact joint form Abaqus are shown in Figure 16.

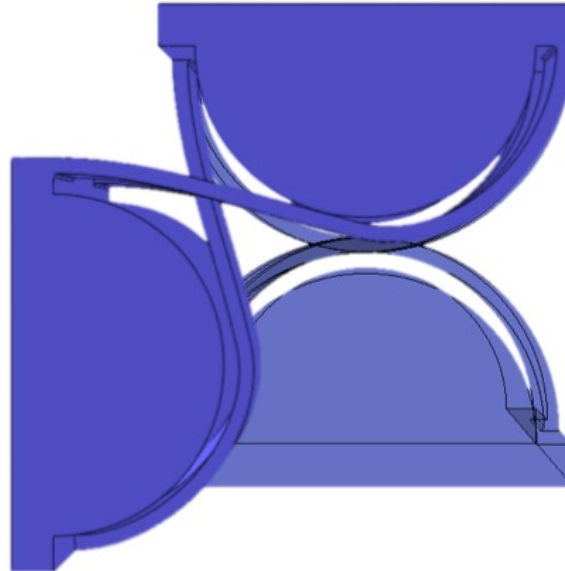


Figure 16. The un-deformed (transparent blue) and deformed (solid blue) states of the contact model in the Abaqus simulation are shown.

Unlike the cross axis hinge, the analytical and numerical calculations for the contact bearing did not match. The maximum stress for the ABS contact bearing varied between 95.11 and 96.43 MPa, which gave a percent error of over six hundred percent. As with ABS, the nylon contact bearing had percent errors over six hundred percent, with stresses from 27.13 to 27.50 MPa. The smallest stresses for both ABS and nylon occurred in the mesh of 1 mm (Figure 17), where the maximum stress is both cases was located middle of the center flexural arm, respectively.

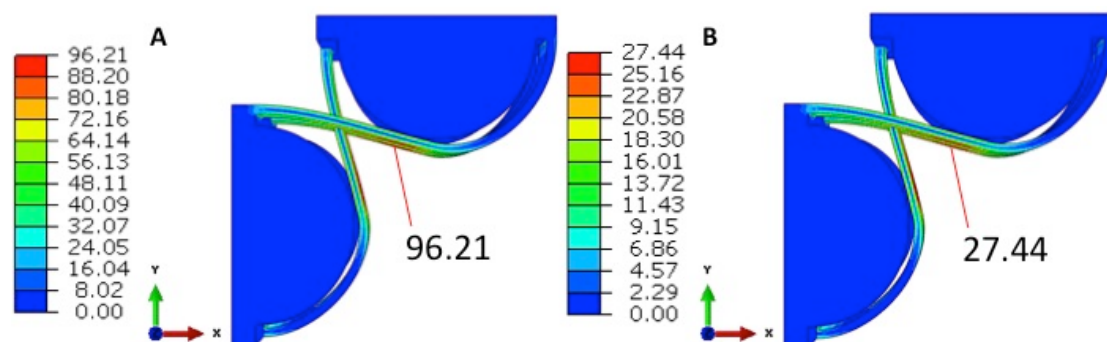


Figure 17. With a deflection of ninety degrees, the contact bearing has a maximum von Mises stress of A) 96.21 MPa in ABS and B) 27.44 MPa in nylon.

	Global Seed Size (mm)	Maximum Stress (MPa)	Strain Energy Density (mJ/mm ³)	Analytical Stress (MPa)	Error (%)
ABS	1.4	96.43	57.21	13.27	626.68
	1.0	95.11	57.07	13.27	616.73
	0.8	96.21	57.03	13.27	625.02
Nylon	1.4	27.50	16.32	3.78	627.51
	1.0	27.13	16.28	3.78	617.72
	0.8	27.44	16.27	3.78	625.93

Table 8. The mesh convergence study for the contact bearing made of ABS and Nylon, where the results show that as the element size is decreased, the simulations start to converge to a solution. With the smallest mesh size, the percent error between the analytical and numerical solutions is over six hundred percent.

As can be seen in Table 8, the stress calculated analytically does not match the numerical stress calculations, with differences of over six hundred percent. Due to these substantial differences between the calculated stresses, it seems that the analytical calculations are inaccurate and do not accurately represent the stresses that occur during the deflection of the contact bearing. Despite the difference in calculated stresses, the design in nylon did not experience yield in both the analytical and numerical calculations. On the other hand, the ABS design experienced stresses over double the yield stress. Since the design in ABS experienced yield stresses, this design was no longer an option to use for testing since both materials should not undergo plastic deformation.

2.4.3 Spiral

In the spiral design, two spiral springs are connected by a rod whose centerline is coincident with the axis of rotation. The spring design has both high levels of compliance and deformation that aid in achieving large deflections [89]. The maximum stress in flat spiral springs can be calculated using equations from machine design theory, where both geometrical and material factors affect the maximum stress (Figure 18) [89, 90].

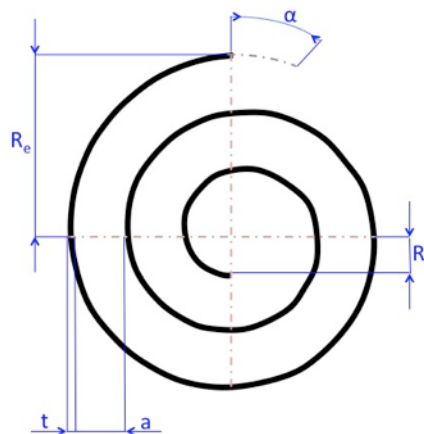


Figure 18. A diagram of the spiral that shows the dimensional variables.

The induced stress is calculated using this equation:

$$\sigma = \frac{6 \cdot M}{b \cdot t^2} \quad (11)$$

where M is the loading of the spring, b is the width of the spring strip, and t is the thickness of the spring strip. In addition to the stress, the maximum angular deflection, α , is calculated with:

$$\alpha = \frac{12 \cdot 180 \cdot M \cdot L}{\pi \cdot E \cdot b \cdot t^3} \quad (12)$$

where L is the functional spring length and E is the young's modulus. The functional spring length is a function of R_e , the outer radius of the spring, R_i , the inner radius of the spring, t , and a , the space between the spring coils:

$$L = \frac{\pi(R_e^2 - R_i^2)}{a + t} \quad (13)$$

Combining equations 11-13, the variables can be rearranged to solve for the maximum stress in terms of the deflection angle:

$$\sigma = \frac{\alpha \cdot E \cdot t(a + t)}{360(R_e^2 - R_i^2)} \quad (14)$$

With a deflection angle of ninety degrees, MATLAB was utilized to create a plot of the maximum spiral stress as a function of coil thickness (Appendix A). The chosen minimum and maximum coil thickness were 0.5 mm and two mm, respectively. An angular deflection of ninety degrees was used, as well as the material properties for ABS and Nylon previously mentioned. The plots showed that there were coil thicknesses that resulted in stresses below the yield point for both ABS and Nylon (Figures 19 and 20). For ABS, the maximum possible coil thickness is 1.63 mm, while for Nylon the spiral did not experience any yielding for any coil thickness below two mm.

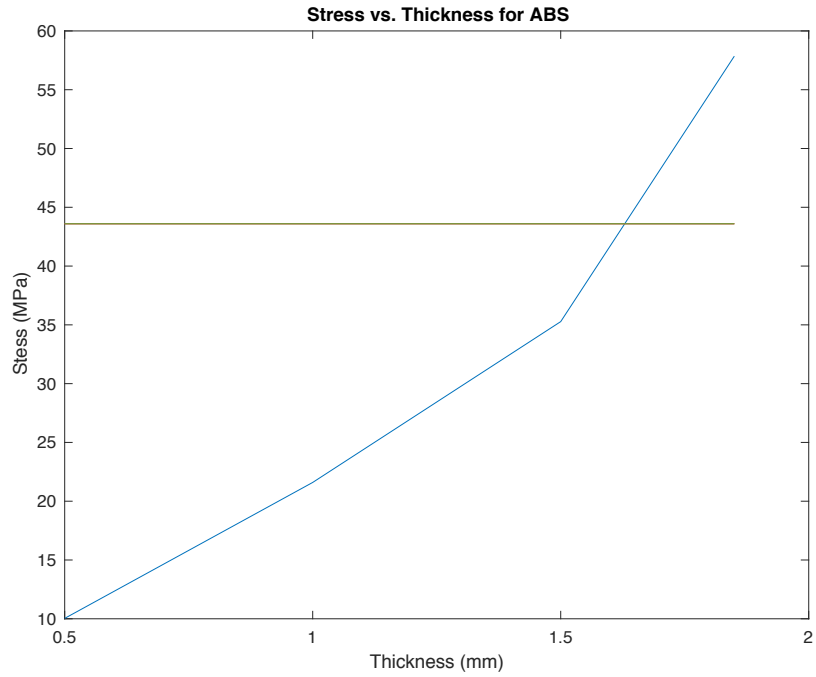


Figure 19. A plot of the coil thickness of the spiral versus the maximum stress in the spiral made of ABS.

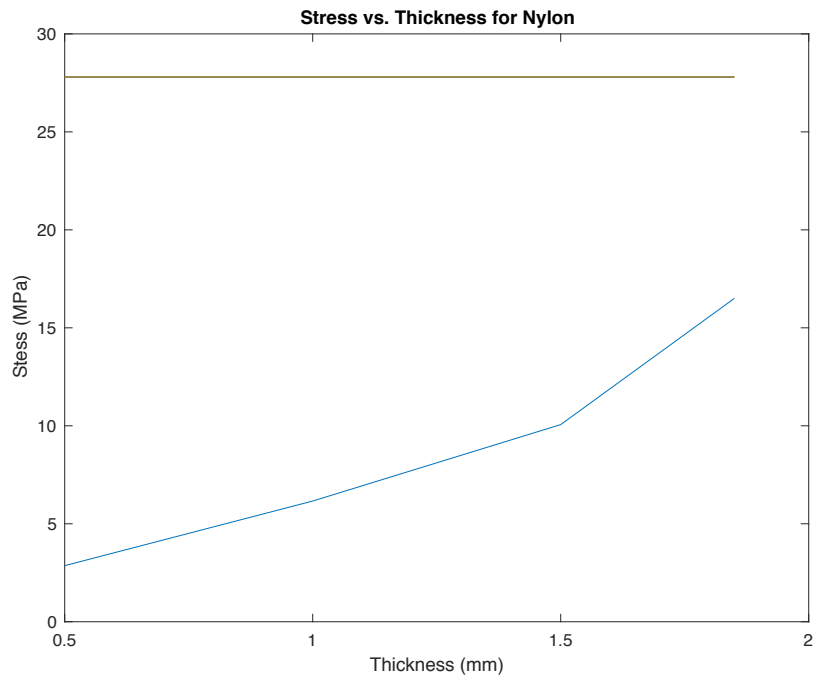


Figure 20. A plot of the coil thickness of the spiral versus the maximum stress in the spiral made of Nylon.

Using the minimum coil thickness of 0.5 mm, a new plot was created to show the maximum stress values over the entire deflection range of zero to ninety degrees for ABS and Nylon (Figures 21 and 22).

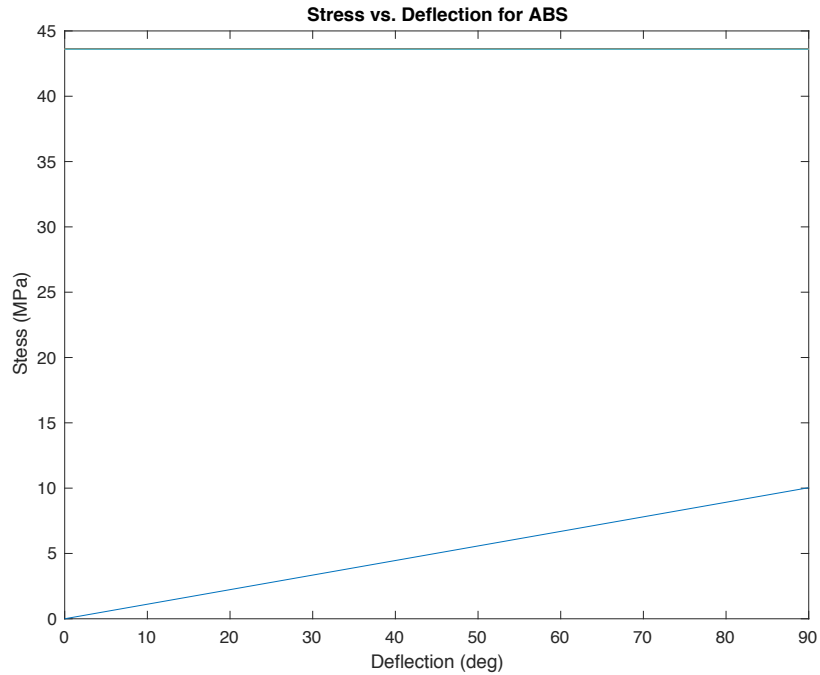


Figure 21. This plot shows the maximum stress of the ABS spiral as a function of the deflection angle from zero to ninety degrees.

Throughout the entire range of motion, both ABS and Nylon do not experience yield stresses (Figures 21 and 22), with the maximum stress occurring at ninety degrees. At ninety degrees, the maximum stress in ABS is 7.48 MPa, which is 31.70 MPa below yielding. For Nylon, the maximum stress at ninety is almost 25 MPa below the yield stress.

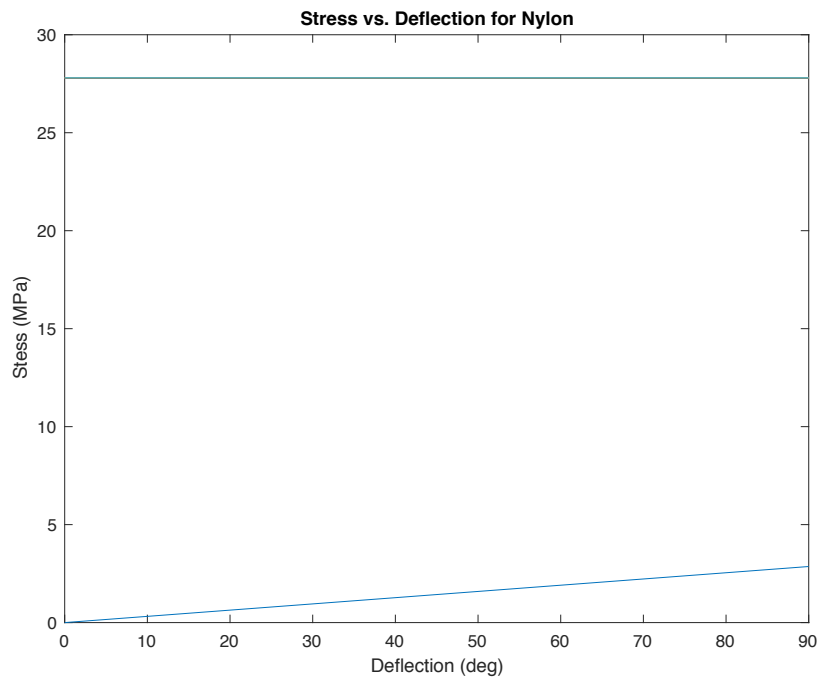


Figure 22. This plot shows the maximum stress of the Nylon spiral as a function of the deflection angle from zero to ninety degrees.

As with the previous two designs, a finite element model was created using Abaqus to verify the analytical stress calculations. The same material properties, boundary conditions, and mesh elements were applied to the model. Instead of using global seed elements to mesh the entire joint, as was done previously, seed edges were applied to the spirals themselves. This was done so that the spirals were the only section of the part to experience a change in element size. The deformed and un-deformed states of the spiral in the numerical simulation are shown in Figure 23. As well, a mesh convergence study was completed (Table 9).

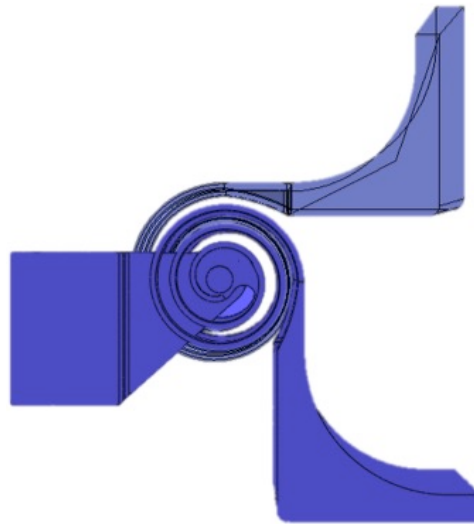


Figure 23. The un-deformed (transparent blue) and deformed (solid blue) states of the spiral joint in the Abaqus simulation are shown.

	Spiral Seed Elements	Maximum Stress (MPa)	Strain Energy Density (mJ/mm ³)	Analytical Stress (MPa)	Error (%)
ABS	150	16.12	1.81	10.10	59.60
	200	15.17	1.8	10.10	50.20
	250	18.29	1.81	10.10	81.09
Nylon	150	4.6	0.52	2.90	58.62
	200	4.33	0.51	2.90	49.31
	250	5.22	0.52	2.90	80.00

Table 9. The mesh convergence study for the spiral made of ABS and Nylon, where the results show that as the element size is decreased, the simulations start to converge to a solution. With the smallest mesh size, the percent error between the analytical and numerical solutions is over six hundred percent.

The maximum stresses seen in the ABS and nylon designs varied between 16.12 and 18.29 MPa, and 4.6 and 5.22 MPa, respectively. From these calculated values, the error between the analytical numerical model was consistently around fifty percent or higher. In the case of 200 spiral elements, the maximum stress was the lowest. The ABS case had a stress of 15.17 MPa and the nylon case had a stress of 4.33 MPa (Figure 24). Both materials experienced the maximum stress in the same location: the connection between the inner spiral and the axle.

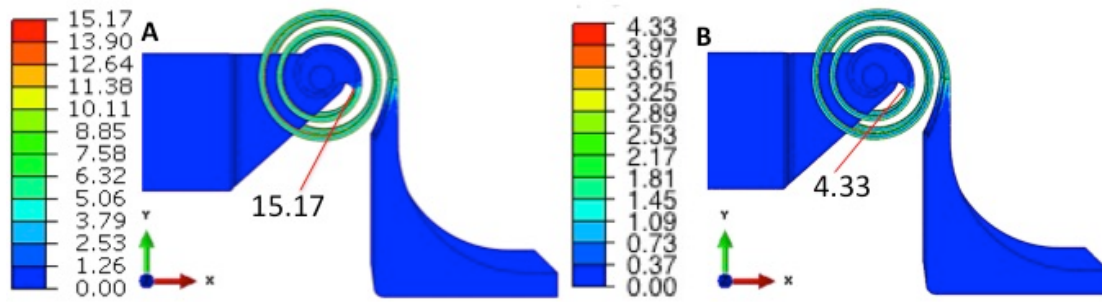


Figure 24. With a deflection of ninety degrees, the spiral has a maximum von Mises stress of A) 15.17 MPa in ABS and B) 4.33 MPa in nylon.

The stress calculated analytically was consistently smaller than the numerical stress, which may be a result of misestimating the stress concentration factor of the spirals, since the equations were made for an idealized spring. Despite the large errors between the two solutions, the spring does not experience yield stress in both the analytical and numerical analyses. Due to the spiral joint not experiencing plastic deformation during deflection for both materials, it was still in consideration for testing.

2.4.4 Final Designs

From the analytical and numerical analyses of the several joint designs, two were chosen to undergo fatigue testing: the cross axis hinge and the spiral. These were chosen due to the fact that the two designs did not experience yield stresses over the full range of motion for both ABS and Nylon. The contact bearing was not chosen since the analytical and numerical calculations did not match, and the numerical model predicted loads above yield stress when the joint deflected across the desired range of motion.

For the final two designs, a circular arc was added to the ends of the joint, as can be seen in Figure 25. This was a result of the chosen fatigue testing method. For fatigue testing, it was decided that axial loading would be applied, which meant that the axial motion of the testing machine would need to be translated into circular motion in order to achieve the rotational motion of the joints. The circular arc allowed the joint designs to deflect along a circular path, despite the axial motion of the fatigue testing press.

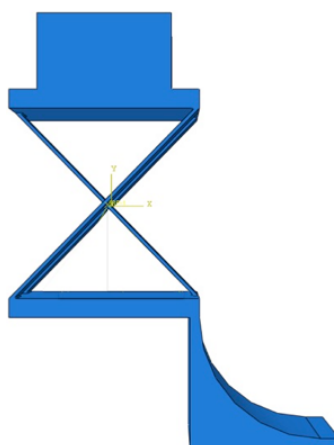


Figure 25. This figure shows the final addition to the designs, the circular arc.

2.5 Printing Parameters

When printing the specimens, certain printing parameters were taken into consideration, while others were left to their default values. First, infill density, build plate temperature, nozzle temperature, and nozzle speed were left at their default values set by Ultimaker for the specific materials. The temperature and speed variables were also left to their default values because those were the recommended settings from Ultimaker for the best print quality. The infill density was not taken into consideration because the infill density would not have had a direct effect on the flexure arms or spiral due to their small size. On the other hand, variables such as printing orientation, support density, and built plate adhesion were taken into account. The specimens were printed flat on their side so that the fibers were in alignment with how the joints would be rotating (Figure 26). In the figure below, the build plate is coincident with the XY plane.

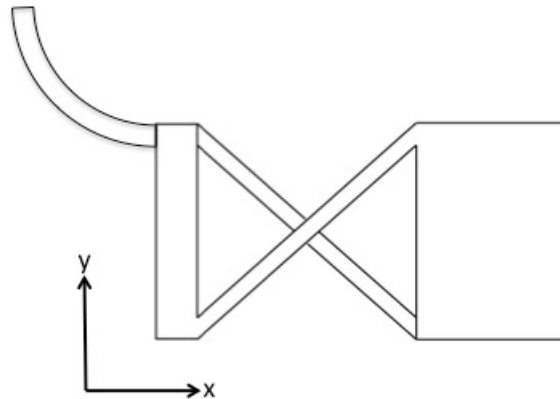


Figure 26. This shows the printing orientation of the final designs on the build plate, where the part is laying flat on the build plate so that the deflection of the part is coincident with the fiber orientation.

If the joints were printed in a different orientation, then the fibers would be in misalignment with how the joint should deflect. This misalignment would prevent the joints being as strong as they could be, since the fibers would not bend in alignment with the deflection. Next, due to the chosen printing orientation, there needed to be support material. Without support material, both the cross axis hinge and spiral designs would collapse. The default support material pattern was chosen since the structures that required support were too small for the pattern to have an influence. In order to improve the adhesion between the part and the support material, the support density was increased by fifteen percent from the default value. Finally, the build plate adhesion was taken into consideration since it was essential that the joint designs stick to the build plate. If the part were to peel up from the build plate, then the part would either partially or completely fail at the end of printing. For ABS, a raft was used, as it was found through trial and error that the ABS parts had the best quality with a raft. With nylon, a brim layer was used in addition to translating the part one mm off the build plate. This translation was performed so that a layer of support material would be deposited underneath the part. This thin support material layer prevented the brim layer from fusing together with the spiral, and preventing good print quality.

2.6 Testing Setup

The system used for fatigue testing was the Instron ElectroPlus™ E10000 Test System, which is able to apply either an axial or torsional load to a specimen. As previously mentioned, axial loading was chosen instead of torsional loading as a result of the joint geometry. In this fatigue testing, the Instron would also apply a displacement, not a force, to the specimens.

2.6.1 Clamping Stand

In order for a displacement to be applied to the specimens, a stand had to be manufactured to clamp the specimen while the Instron press moved vertically along its predefined path. The clamping stand was designed in Solidworks using the dimensional specifications of the Instron machine and the geometry of the joint designs (Appendix B). There were two sections to the clamping stand: the base and the tower. The base connects the clamping stand to the Instron machine, the base and tower are connected using screws, and the tower holds the specimen in place with screws (Figure 27).

The clamping stand was fabricated using a milling machine and was made out of aluminum. M10 slots, 160 mm apart, were designed into the base with 15 mm of leeway. Slots were used since the two joint designs were different lengths, and the leeway allowed the stand to be adjustable depending on which design was being tested. On the top of the stand tower, three holes were machine above where the part would be clamped. The holes allowed the specimens to be clamped down using screws, which ensured that the specimens would not move during testing.

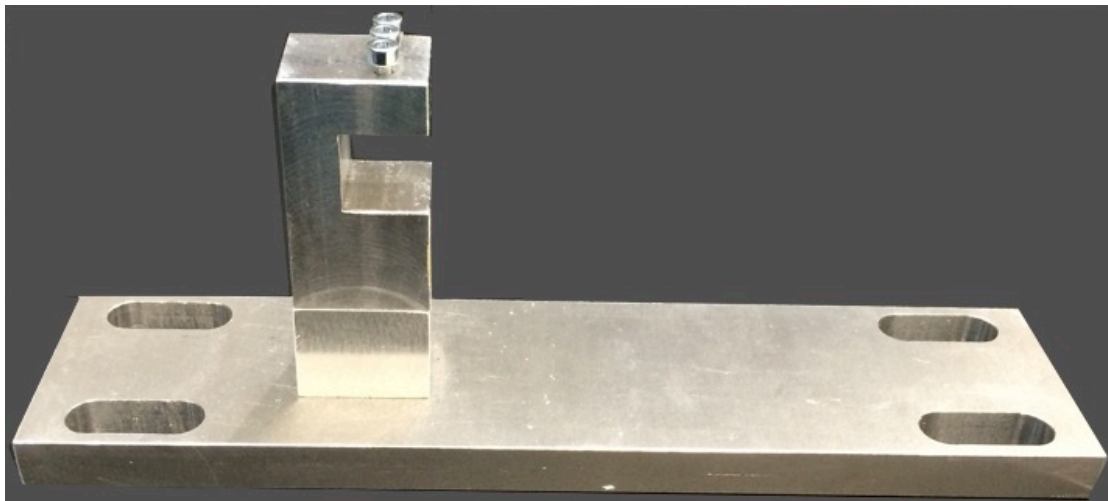


Figure 27. This figure is zoomed into show the clamping stand base and tower, which attaches the clamping stand to the Instron and holds the sample in place while testing. The screws that attach the clamping stand to the Instron are now shown in this picture

In addition to the clamping stand, a press had to be designed to push the specimens down to the desired angle (Appendix B). The top portion of the press, also made of aluminum, was cylindrical in shape and had M6 threads at one end, which would attach the press to the Instron load cell. At the opposite end from the threads, a hemispherically steel piece was glued to the press using a metal-on-metal epoxy. The bottom end of the press was designed to be spherically shaped so that there was

always only one point of contact between the press and the compliant joint. The final setup with the base, tower, and press is shown below in Figure 28.

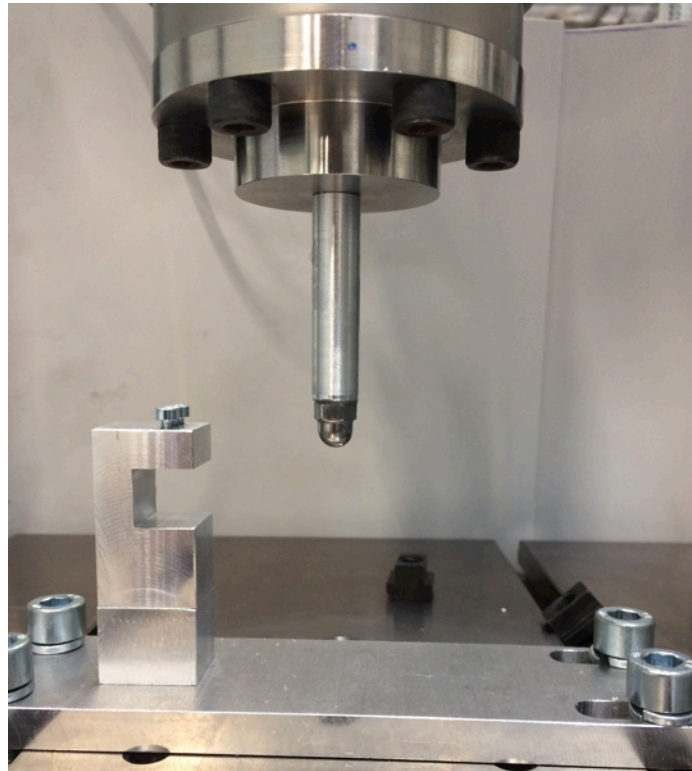


Figure 28. In this picture, a schematic overview of the test setup is shown. The base of the clamping stand is connected to the Instron with screws. The tower and the base are connected by screws (not seen in this picture), and the press is connected to the load cell of the Instron. The specimen would be held in the tower of the clamping stand with the three screws located on its top.

2.6.2 Instron Settings

After installing and calibrating the Instron load cell, the clamping stand and press were attached to the testing bench and load cell, respectively. With the press installed, the load cell was zeroed, and a sample specimen was placed into the tower. The press was displaced vertically until barely touching the specimen. This point was taken to be the maximum point in the cyclic displacement of the press. The minimum point of the loading cycle was when the specimen was displaced the full ninety degrees. The distance between the minimum and maximum points was first approximated through the numerical model, and then adjusted visually when testing the Instron machine. Using the minimum and maximum points of the joint rotation, the Instron was programmed to cyclically move between these two points.

The Instron program began by moving the press to the zero point of the cycle, which was defined as halfway between the minimum and maximum points. Once the press was moved to the zero point, the Instron was set to cyclically displace between the minimum and maximum points at 0.5 hertz. The cycle limit was set to 100,000 cycles. According to ASTM, it is recommended to test plastics below five hertz in order to avoid temperature effects by reducing heat generation while testing [20]. Breaking from traditional fatigue testing, a 100,000 cycle limit was set instead of one million since upper-limb prostheses are estimated to use over 100,000 cycles annually [91].

The testing stopped once the specimen broke or reached the cycle limit, and the press returned to the zero position.

2.7 Testing

The testing was set up so that each of the two designs was tested in both ABS and nylon using a deflection of ninety degrees. For each combination, three specimens were tested to examine the repeatability of the results. A break in the specimen was defined as a complete fracture of the specimen, not when the specimen began to undergo plastic deformation.

3 Results

3.1. First Test Iteration

During the first round of fatigue testing, several modifications were made to both designs. First focusing on the spiral design, the spiral was not strong enough to hold up its own body weight. As a result of this, no specimens were tested in this iteration. Since the spiral was unable to maintain its shape under its own weight, the joint deflected to an angle of twenty-four degrees instead of resting at zero degrees (Figure 29). Due to this displacement, the design was changed to make the spirals three times thicker, 1.5 mm, so that they would be stronger.

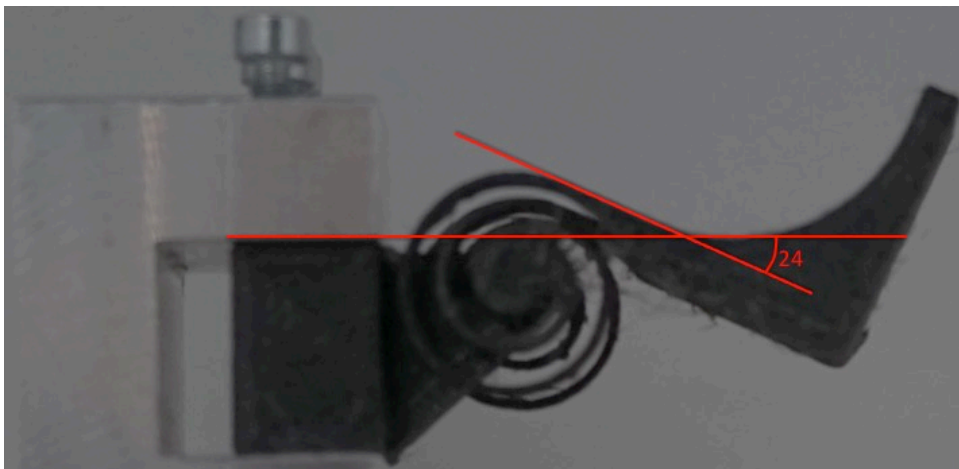


Figure 29. The deflection of the nylon spring design, 0.5 mm coil thickness, under its own body weight.

Looking at the cross axis hinge design, one specimen for the cross axis hinge in ABS was tested (Table 10, Appendix C). The joint was not stiff enough for the Instron to detect when a fracture occurred during fatigue testing. This was a result of the load cell being unable to detect loads smaller than 40 N accurately. In order to increase the stiffness, the width of the flexural arms was doubled to eight mm, since the width should not have an impact on the maximum stress experienced by the joint.

Design	Material	Number of Cycles	Fracture Location
Cross Axis Hinge	ABS	3500	One fracture location in the center of the middle flexural arm

Table 10. The maximum number of cycles achieved during fatigue testing and the fracture location on the cross axis hinge, four mm width, in ABS.

3.2. Second Test Iteration

In the second round of iterations, both designs again underwent alterations. For the spiral design, three specimens underwent fatigue testing (Table 11, Appendix D). During testing, it was observed that the pitch between the spirals was too small and that the coils were interfering with one another during deflection. As a result of the interference, the pitch was increased from 1.25 mm to 1.7 mm.

Design	Material	Number of Cycles	Fracture Location
Spiral	ABS	1000	The left axle of the specimen broke
		2400	The outside right spiral fractured in the middle of the left side
		4555	The outside right spiral fractured in the middle of the left side

Table 11. The maximum number of cycles achieved during fatigue testing and the fracture location on the spiral, 0.5 mm thickness, in ABS.

Despite having doubled the width of the cross axis hinge, the Instron was still unable to detect when a fracture occurred since the joint was not stiff enough. Since the doubled width did not improve the fracture detection, the width of the flexural arms was decreased to six mm to remain within the size constraint. One sample with a width of eight mm was tested (Table 12, Appendix D).

Design	Material	Number of Cycles	Fracture Location
Cross Axis Hinge	ABS	5800	There were three fracture locations at ends of the flexural arms

Table 12. The maximum number of cycles achieved during fatigue testing and the fracture location on the cross axis hinge, eight mm width, in ABS.

3.3. Third Test Iteration

Once the final geometry alterations were completed, the final designs of the cross axis hinge and spiral were tested. Along with the fatigue testing, a final numerical model and mesh convergence study were completed to verify that the designs did not experience yield stress.

3.1.1 Cross Axis Hinge

In order to ensure that the final designs did not undergo yield stress over the deflection range, a numerical model was set up in the same way as previously. Since the analytical calculations were unaffected for the cross axis hinge, the same stress values were used when determining the error between the two models. For the numerical model, a mesh convergence study was completed (Table 13). As seen in Table 13, as the mesh became smaller, the simulations started to converge to a solution. The smallest stresses for both ABS and nylon occurred in the models with the 0.8mm element size, with the maximum stress occurring at the connection between the flexural arms and the base (Appendix E). The error between the numerical and analytical models, for both ABS and Nylon, was less than ten percent in the case of the smallest element size.

	Global Seed Size (mm)	Maximum Stress (MPa)	Strain Energy Density (mJ/mm ³)	Analytical Stress (MPa)	Error (%)
ABS	1.4	48.96	5.01	43.17	13.41
	1.0	75.86	5.11	43.17	75.72
	0.8	40.55	4.99	43.17	-6.07
Nylon	1.4	12.69	1.41	12.31	3.09
	1.0	23.36	1.43	12.31	89.76
	0.8	13.21	1.41	12.31	7.31

Table 13. The mesh convergence study for the cross axis hinge made of ABS and Nylon, where the results show that as the element size is decreased, the simulations start to converge to a solution. With the smallest mesh size, the percent error between the analytical and numerical solutions was less than ten percent.

During fatigue testing, three specimens of ABS and Nylon were tested, where the number of completed cycles and the fracture locations were recorded in Table 14 (Appendix F). Focusing on the ABS samples, the number of cycles that the samples underwent before fracture was minimal. Two of the three specimens failed below 5000 cycles, and the final sample failed below 6000.

Material	Number of Cycles	Fracture Location
ABS	4500	The middle flexural arm fractured in the center
	4350	The middle flexural arm fractured in the center
	5750	The left flexural arm fractured at the bottom connection
Nylon	100000	There was not fracture during the testing
	100000	There was not fracture during the testing
	100000	There was no fracture during the testing

Table 14. The maximum number of cycles achieved during fatigue testing and the fracture location of the cross axis hinge, six mm width, in ABS and Nylon. There were three samples for each material.

All three ABS samples fractured in the center of the middle flexural arm (Figure 30, Appendix F). During testing, all of the ABS samples were able to return to their original positions each cycle and did not experience creep behavior.

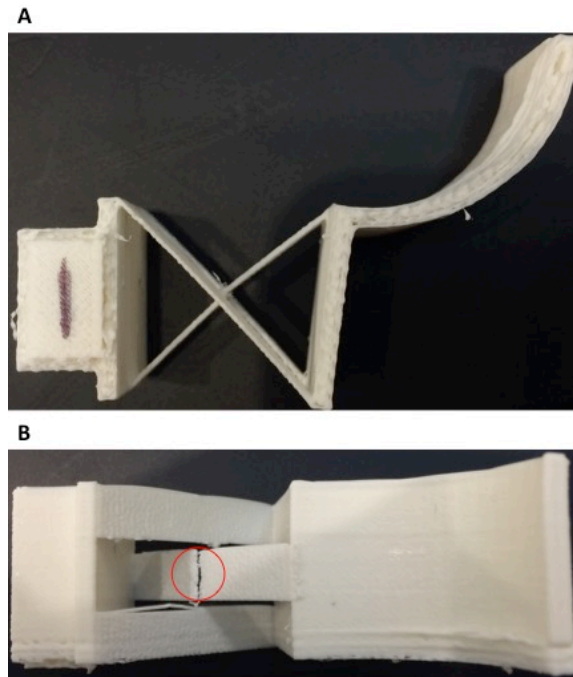


Figure 30. The first cross axis hinge sample made of ABS, 6 mm width, which was fatigue tested. After fatigue testing, A) the front view and B) top view can be seen. In the top view, the fracture location can be seen in the middle flexural arm

In comparison with the ABS samples, all of the nylon samples did not fracture before the 100,000 cycle limit (Figure 31). Even though the nylon samples did not fracture, they seemed to experience creep throughout fatigue testing. After 100,000 cycles, the samples were deflected from their original positions by an average of 19.7 degrees (Figure 32).

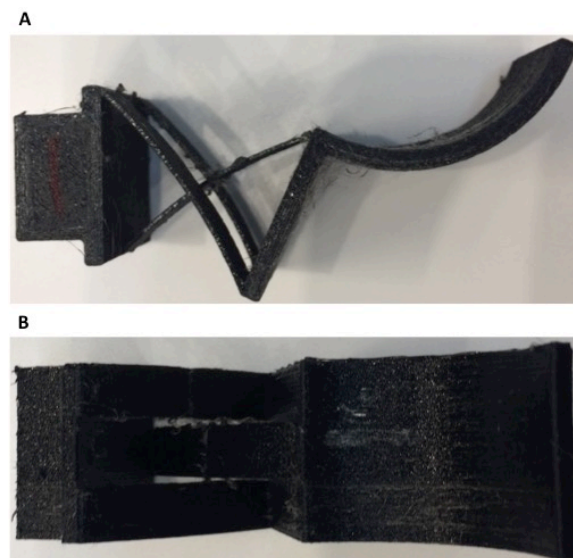


Figure 31. The first cross axis hinge made of Nylon, 6 mm width, which was fatigue tested. After fatigue testing, A) the front view and B) top view can be seen. In the front view, it can be seen that the nylon was unable to return to its original shape.

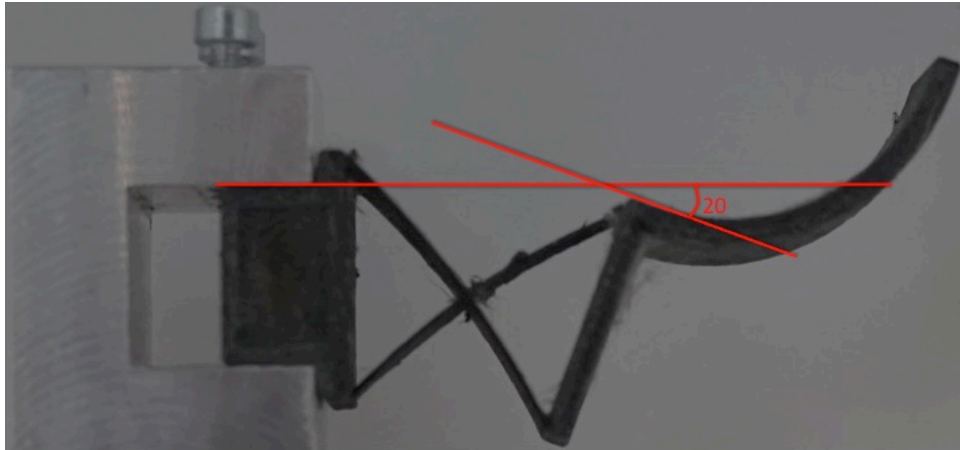


Figure 32. The front view of the first cross axis hinge sample, 6 mm width, after fatigue testing while still being held in the fixture. The sample was unable to return to its original position by angle of twenty degrees.

3.1.2 Spiral

Similarly to the cross axis hinge, a numerical model and mesh convergence study were completed for the spiral, in addition to an updated analytical calculation (Appendix G). In the numerical simulations, the maximum stress was seen at the transition between the inner spiral and the axle (Appendix H). From the mesh convergence study, as the number of elements increased in the spiral, the model began to converge (Table 15). At the smallest mesh size, the percent difference between the models is less than eleven percent for both materials.

	Spiral Seed Elements	Maximum Stress (MPa)	Strain Energy Density (mJ/mm ³)	Analytical Stress (MPa)	Error (%)
ABS	100	45.96	45.79	39.05	17.70
	200	43.56	45.79	39.05	11.54
	250	43.18	45.76	39.05	10.58
Nylon	100	12.22	13.04	11.14	9.69
	200	12.27	13.04	11.14	10.14
	250	12.36	13.04	11.14	10.95

Table 15. The mesh convergence study for the spiral made of ABS and Nylon, where the results show that as the element size is decreased, the simulations start to converge to a solution. With the smallest mesh size, the percent error between the analytical and numerical solutions was less than eleven percent.

The samples that were tested in ABS all fractured within 7000 cycles, where the worst and best samples failed at 3800 and 7000 cycles, respectively (Table 16, Appendix I).

Material	Number of Cycles	Fracture Location
ABS	3800	There were two fractures in the right spiral, with one at the top of the outer spiral and one on the right side of the middle coil
	5550	There was one fracture on the right spiral in the outer coil in the middle of the right side
	7000	There was one fracture on the right spiral in the outer coil in the middle of the bottom side
Nylon	100000	There was not fracture during the testing
	100000	There was not fracture during the testing
	100000	There was no fracture during the testing

Table 16. The maximum number of cycles achieved during fatigue testing and the fracture location of the spiral, 1.5 mm thickness, in ABS and Nylon. There were three samples for each material.

Consistently in the ABS samples, the fracture occurred in the spiral that was not in contact with the build plate during printing, also known as the right spiral. In the three specimens, there were either one or two fractures in the outermost two coils (Figure 33, Appendix I).

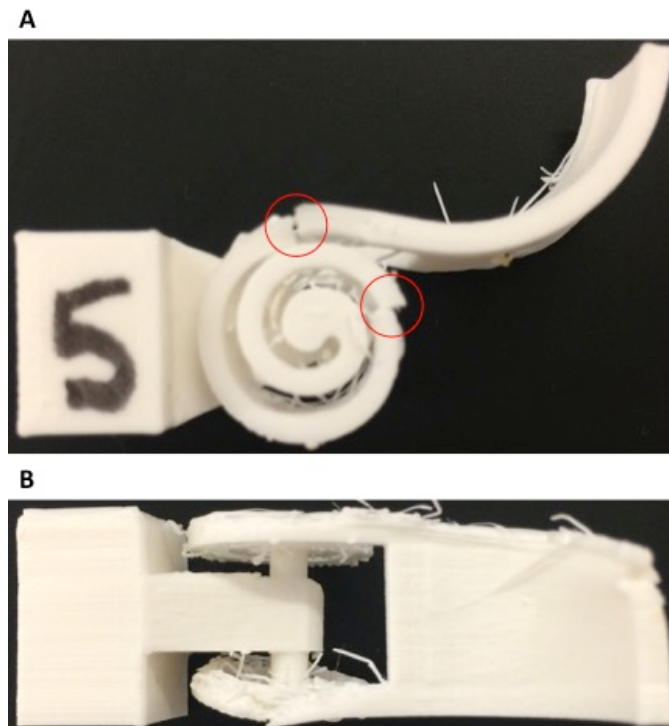


Figure 33. The first spiral made of ABS which was fatigue tested. After fatigue testing, A) the front view and B) top view can be seen. In the front view, it can be seen that there were two fractures in the right spiral on the top and right sides of the outer spiral.

In the spiral design, all three of the nylon samples did not fracture before the 100,000 cycle limit (Figure 34). Similar to the nylon cross axis hinge, the spiral was also unable to return to its original shape after fatigue testing by an average of sixteen degrees (Figure 35).

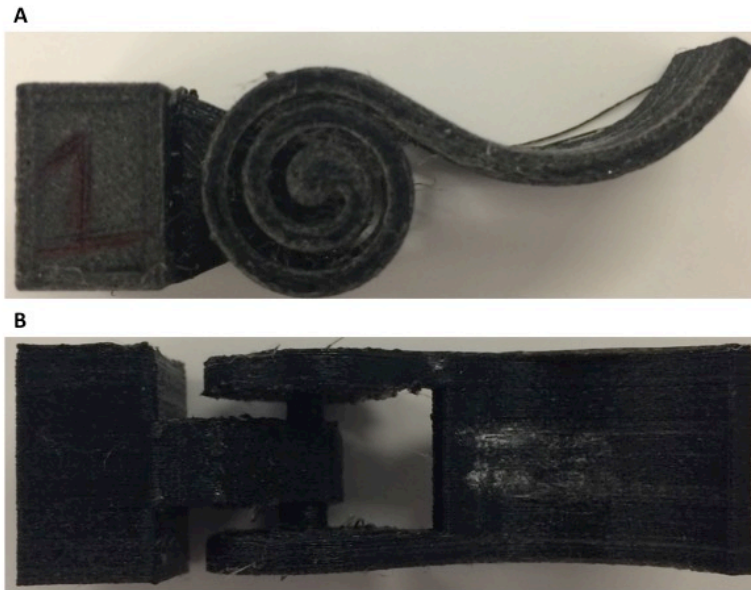


Figure 34. The first spiral made of nylon which was fatigue tested. After fatigue testing, A) the front view and B) top view can be seen. In the front view, it can be seen that the nylon was unable to return to its original shape.

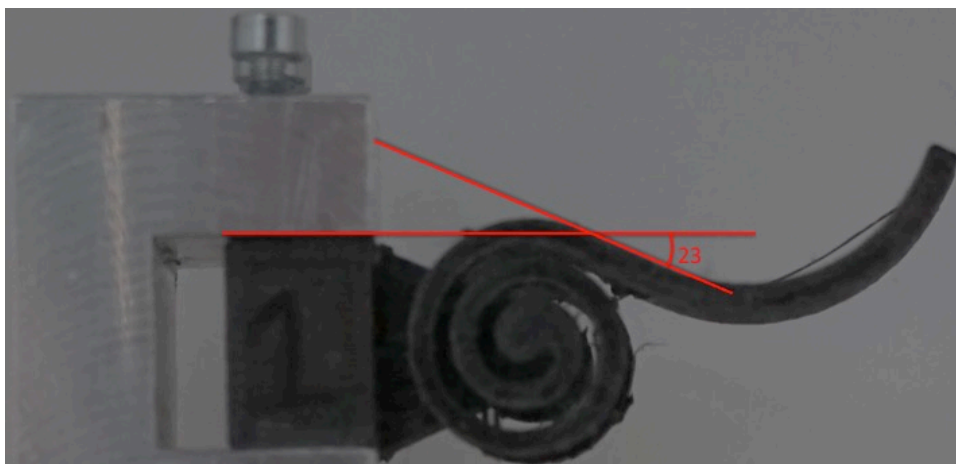


Figure 35. The front view of the first spiral sample, after fatigue testing, while being held in the clamp. The sample was unable to return to its original position by an angle of twenty-three degrees.

4 Discussion

The aim of this thesis was to explore the fatigue life properties of two different compliant joint designs and to investigate the applicability of two materials in fatigue situations. Compliant joint designs were first chosen based on their degrees of freedom, range of motion, and size. Both analytical and numerical models were created in order to analyze the maximum stress experienced by the joints, and to check that the specimens did not experience yield. The joints were then optimized and printed, before commencing with fatigue testing.

4.1 Analytical and Numerical Model Comparison

Two model types were utilized to analyze the maximum stress experienced by the four combinations of joint designs. The analytical model assumed that the materials were linear elastic and homogenous. In order to validate the analytical model, a numerical model was also created using a finite element model. The numerical model conformed to the assumptions made by the analytical model. In the analytical models, it was assumed that the materials were linear elastic and homogenous, which is a simplification in the case of 3D printing since the specimens would be anisotropic and inhomogeneous in reality. The maximum stress predicted by the analytical and numerical models for the cross axis hinge and spiral, in both materials, were within eight and eleven percent of each other, respectively. Since the final maximum stress predicted by the two models were within eleven percent of each other, it validated the results obtained with the analytical model.

4.2 Material Behavior

Upon initial observation, there was a clear difference in the material behavior between the ABS and nylon samples. When focusing on the number of cycles throughout testing, all of the nylon samples completed the full 100,000 cycle limit, while the ABS samples were all below 7,000 cycles, for both the cross axis hinge and spiral. From solely the number of cycles, it can be deduced that nylon is the more fatigue resistant material since it is able to undergo testing without breaking or fracturing. During testing, the ABS samples experienced instantaneous fractures, while the Nylon samples underwent permanent deformation. Polymers are viscoelastic materials; this means that they have both viscous and elastic properties, and they are strain-rate dependent. If continuous stress is applied to viscous materials, such as during fatigue testing, the strain will continually increase. Under constant stress, the nylon samples began to experience creep, which is the tendency of a material to permanently deform. In ductile materials, like nylon, failure first begins with yielding before complete disentanglement of the polymer chains. On the other hand, in brittle materials, like ABS, localized disentanglement takes place before yielding. Throughout the fatigue testing, the nylon samples began to plastically deform within the first thousand cycles and progressively underwent worse deformation until the average deflection of the cross axis hinge and spiral were 19.7 and 16 degrees, respectively. As the samples deflected more from their original positions, the samples gradually became unable to function properly across the desired range of motion. Unlike the nylon samples, the ABS samples experienced very rapid cracking, making their failure unexpected and

unpredictable. As previously stated, the nylon samples had better fatigue life, but both nylon and ABS did not have good functionality for the application of the hand prosthesis. The ABS samples failed after a few thousand cycles, while the nylon samples deformed to the point that they were unable to perform the desired function.

In the comparison of the two models with the experimental results, the calculated maximum stress from the analytical and numerical models seemed to provide an adequate prediction for the experiments. In the final designs, the maximum stress for the ABS specimens in the cross axis hinge and spiral were 43.17 and 39.05 MPa, respectively. These stresses are close to the yield stress of 43.6 MPa for ABS. All of ABS failed relatively quickly within 7,000 cycles, which matches the high stresses predicted by the two models. The closer stresses are to the yield stress, the quicker they fail. The stresses predicted for the nylon samples were 12.31 and 11.14 MPa for the cross axis hinge and spiral, respectively. Unlike the ABS samples, these stresses were less than half of the yield stress, 27.8 MPa, for nylon. The low predicted stresses agreed with the results obtained from the nylon samples; all the nylon samples lasted for the full one hundred thousand cycles. Despite being able to speculate that the nylon samples would be able to last for a large number of cycles, the models were unable to predict the creep experienced by the nylon specimens. Both the analytical and numerical models were able to provide results that matched relatively well with the experimental results.

4.3 Geometry Behavior

Aside from the material properties, the geometry of the two different designs was also taken into consideration. As mentioned above, the nylon samples experienced creep behavior throughout fatigue testing, where the average deflection of the cross axis hinge and spiral was 19.7 and 16 degrees, respectively. From these averages, it appears that the spiral design is less affected by creep during testing. After fatigue testing, the nylon spiral samples had a lower average deflection from creep behavior, implying that the strength of the spiral design was greater than that of the cross axis hinge. Due to its larger strength, the spiral design seems to be the better design in terms of fatigue life. When also analyzing the two geometries, the standard deviation of the number of cycles for each design made in ABS was calculated (Table 17).

Joint Design	Range (Cycles)	Mean (Cycles)	Standard Deviation (Cycles)
Cross Axis Hinge	4350-5750	4866.7	627.6
Spiral	3800-7000	5450.0	1308.3

Table 17. The range, mean, and standard deviation calculations for the cross axis hinge and spiral specimens made of ABS

As seen in Table 17, the spiral design had a standard deviation twice as large as the cross axis hinge. Between the two designs in nylon, there weren't any assessable differences in the number of cycles since all of the samples in nylon reached 100,000 cycles. From the standard deviation of the ABS samples, the cross axis hinge had the smaller standard deviation, which could mean that the design itself was more reliable than the spiral design since its results were more closely distributed. This result may also indicate that the spiral design is more susceptible to sources of error than the cross axis hinge. Since the spiral design is more complex geometrically, there are

more variables that could contribute to the performance of the joint. These factors could include the uniformity between the spirals or the quality of the print in terms of support material, build plate heating, or warping. To examine more closely the reliability of the designs, the locations of the fractures in the ABS specimens were investigated. For the cross axis hinge, two of the three designs fractured in the same location: the center of the middle flexural arm. The third specimen fractured at the bottom connection of the left flexural arm. In terms of the spiral specimens, every sample had a different fracture location on the right spiral. Even though the spirals did not break in the same locations, there was consistency with which spiral fractured. This may have been because the right side of the spiral was not in contact with the build plate, and the heat of the build plate did not reach high enough, causing low upper layer adhesion. If the samples had been identical, then the fractures would have occurred in the same location for each sample. Due to the relative consistency in the fracture locations of the cross axis hinge, it implies that the spiral joint is less reliable. Comparing the two geometries from the fatigue testing results, it is difficult to state which one has better fatigue resistance. There was more variation in terms of the number of cycles of the spiral design, but it was effected less by creep. When taking into consideration the application of compliant joints, the creep behavior of the designs is more important since it directly affects the functionality of the joints. If the joint is unable to snap back to its original position, then it is incapable of deflecting across the desired range of motion that is necessary for applications such as a prosthetic hand. In this instance, it seems that the spiral joint is more suitable in fatigue conditions since it does not experience as much plastic deformation as the cross axis hinge.

Comparing these results to the numerical model, none of the samples broke where the predicted maximum stress was located. For the cross axis hinge, the maximum stress was predicted to be at the top connection of the left flexural arm, while the maximum stress in the spiral was predicted to be in the inside coil on the right side. While the analytical and numerical models were able to predict relatively well the performance of the materials, it was unable to predict the location of the maximum stress. This may be due to the assumptions of the model that the joints were linear elastic and homogenous, while in reality this is not the case. In order for the numerical model to better predict the maximum stress location, the anisotropy of the material properties and the fiber orientation would have had to be taken into consideration. From the experimental results, the numerical model did not have accurate predictions of where the maximum stress would occur.

4.4 Limitations

Throughout the setup and testing, there were multiple sources of error that could have influenced the outcome of the fatigue testing. First, in both the analytical and numerical calculations, it was assumed that the joints were homogenous, linear elastic materials. When additively manufacturing compliant joints with FDM, there are inevitably printing parameters that make the joints anisotropic and affect its elasticity. Parameters, such as layer thickness, fiber orientation, and air gap, were not taken into consideration in both models. If these parameters had been included, the predicted stresses and their locations would have been affected, possibly making the models more closely match the experimental results. Second, the support material was printed with the same material as the joints themselves, which made removing the support

challenging. During removal, imperfections or stress concentrations could have been caused since the support melted together with the designs themselves. If a different support material had been used, such as PVA that could be washed off, it may have prevented weaknesses in the joint designs prior to fatigue testing. Another source of error could have been the environmental conditions while printing. Nylon in particular is susceptible to moisture since its resin absorbs water from the air. This absorption decreases the strength and stiffness of nylon, which has a substantial impact on its mechanical properties. If the nylon had been printed in an environmentally controlled chamber or dried out in an oven before use, then the material properties of the nylon may have been different. Finally, the inconsistencies in the printing between builds, such as warping or missing layers, ensured that each sample was different from the others. These variances in the samples may have been caused by multiple factors such as uneven heating on the print bed or poor bed adhesion. If there had been consistent builds between each of the samples, the variation between samples may have been decreased.

4.5 Literature Comparison

Since there is limited literature on fatigue testing of additively manufactured compliant joints, comparisons with previous studies is difficult. Focusing first on the fatigue of specimens printed with ABS, every sample in the literature failed before the full 10^6 or one million cycle limit [92-95]. Throughout the literature, the ABS samples did not last over 25,000 cycles depending on the applied stress [92-95]. These findings are consistent with the results of this experiment, since all of the tested samples in ABS fractured before 7,000 cycles. In comparison with the maximum cycle number of one million, 7,000 and 25,000 are in the same order of magnitude. In addition to the number of cycles, it was also found that ABS experiences brittle failure [94]. This is also in line with what was observed during fatigue testing.

For the nylon samples, there were no studies in literature that investigated fatigue of nylon specimens printed using extrusion-based methods. In several studies, looking at nylon samples printed with selective laser sintering (SLS), samples tested at stresses below 20 MPa lasted for the full 10^6 cycles [96-100]. Although the samples of this study were printed using FDM, the findings in the literature are consistent with the behavior of nylon specimens. As well, several studies found that the SLS parts made of nylon experienced ductile failure, which was observed in the nylon samples of this study [88-90]. Overall, the findings from this study are in accordance with literature.

4.6 Future Work

Due to the limited amount of available literature and the restrictive time for fatigue testing in this experiment, future testing is needed in order to determine which material and joint design would be best under fatigue conditions. There are several different experiments that could be explored in order to determine this. Since both ABS and nylon do not perform well under fatigue conditions for different reasons, other materials, such as TPU or reinforced nylon, should be investigated. As previously mentioned, TPU was determined to be the best material for fatigue, but it was not available at the beginning of this experiment. This would provide a better comparison between materials and provide more information on fatigue resistance and creep behavior. In addition to testing other polymer materials, different printing

methods, such as selective laser sintering or material jetting, should be tested. Other printing methods may provide better print quality and uniform material properties, which could be beneficial in terms of fatigue life. In terms of the geometry, different designs should also be tested to determine if there are more fatigue resistant joints than the cross axis hinge and spiral. This analysis, like that with the other materials, would provide more information on what geometry has the best fatigue life. Finally, beyond testing different materials and designs, printing parameters should also be varied to observe if they would have an effect on fatigue. For example, making the layer height smaller or decreasing printing speed may have beneficial effects in terms of fatigue resistance.

5 Conclusion

This master's thesis explored the fatigue life of additively manufactured compliant joints. Four combinations of geometry and materials were fatigue tested using the Instron ElectroPlus™ E10000 Test System. The experimental results provided information about the material and geometrical properties for the samples; it was found that nylon was the superior material in comparison with ABS, and the spiral joint design was better suited for cyclic load conditions than the cross axis hinge. Even though nylon was better for fatigue life and was able to last for the entire one hundred thousand cycles, it still underwent creep behavior throughout testing. While the specimens did not rupture, they experienced permanent deformation that prevented them from performing the desired function every cycle during testing. On the other hand, the ABS designs experienced instantaneous rupture after several thousand cycles. This was also detrimental behavior because it was unpredictable when the samples would break, and the break rendered them unable to function properly. Looking at the geometry, the spiral design in nylon underwent an average deflection of twenty-six degrees, which was smaller than the deflection of thirty-eight degrees experienced by the cross axis hinge due to creep. Over the one hundred thousand cycles, the nylon designs progressively began to deflect until they reached the final permanent deflections. In terms of materials and geometry, none of the joint combinations had the mechanical stability necessary for long-term functionality. Since the designs lacked the strength to withstand the detrimental effects of cyclic loading, integrating these joint designs into a hand prosthesis would not be viable since the designs would be unable to function properly across the entire range of motion for long-term. Throughout the testing, several sources of error could have contributed to the obtained results of the fatigue testing, such as environmental conditions, removal of support material, and printing inconsistencies. Further experiments, such as testing different materials, geometries, and printing parameters, should be explored to investigate which combinations result in the best fatigue life results.

6 References

- [1] Dizon, J. R. C., Espera, A. H., Chen, Q. Y., & Advincula, R. C. (2018). Mechanical characterization of 3D-printed polymers. *Additive Manufacturing*, 20, 44-67. doi:10.1016/j.addma.2017.12.002
- [2] Macdonald, E., Salas, R., Espalin, D., Perez, M., Aguilera, E., Muse, D., & Wicker, R. B. (2014). 3D Printing for the Rapid Prototyping of Structural Electronics. *Ieee Access*, 2, 234-242. doi:10.1109/Access.2014.2311810
- [3] Bakarich, S. E., Gorkin, R., Panhuis, M. I. H., & Spinks, G. M. (2014). Three-Dimensional Printing Fiber Reinforced Hydrogel Composites. *Acs Applied Materials & Interfaces*, 6(18), 15998-16006. doi:10.1021/am503878d
- [4] Ifkovits, J. L., & Burdick, J. A. (2007). Review: Photopolymerizable and degradable biomaterials for tissue engineering applications. *Tissue Engineering*, 13(10), 2369-2385. doi:10.1089/ten.2007.0093
- [5] Kalita, S. J., Bose, S., Hosick, H. L., & Bandyopadhyay, A. (2003). Development of controlled porosity polymer-ceramic composite scaffolds via fused deposition modeling. *Materials Science & Engineering C-Biomimetic and Supramolecular Systems*, 23(5), 611-620. doi:10.1016/S0928-4931(03)00052-3
- [6] Melchels, F. P. W., Feijen, J., & Grijpma, D. W. (2010). A review on stereolithography and its applications in biomedical engineering. *Biomaterials*, 31(24), 6121-6130. doi:10.1016/j.biomat
- [7] Morris, V. B., Nimbalkar, S., Younesi, M., McClellan, P., & Akkus, O. (2017). Mechanical Properties, Cytocompatibility and Manufacturability of Chitosan:PEGDA Hybrid-Gel Scaffolds by Stereolithography. *Annals of Biomedical Engineering*, 45(1), 286-296. doi:10.1007/s10439-016-1643-1
- [8] Murphy, S. V., & Atala, A. (2014). 3D bioprinting of tissues and organs. *Nature Biotechnology*, 32(8), 773-785. doi:10.1038/nbt.2958
- [9] Rengier, F., Mehndiratta, A., von Tengg-Kobligk, H., Zechmann, C. M., Unterhinninghofen, R., Kauczor, H. U., & Giesel, F. L. (2010). 3D printing based on imaging data: review of medical applications. *International Journal of Computer Assisted Radiology and Surgery*, 5(4), 335-341. doi:10.1007/s11548-010-0476-x
- [10] Wu, G. H., & Hsu, S. H. (2016). Review: Polymeric-Based 3D Printing for Tissue Engineering (vol 35, pg 285, 2015). *Journal of Medical and Biological Engineering*, 36(2), 284-284. doi:10.1007/s40846-015-0069-9
- [11] Liu, R., Wang, Z., Sparks, T., Liou, F., & Newkirk, J. (2017). Aerospace applications of laser additive manufacturing. *Laser Additive Manufacturing: Materials, Design, Technologies, and Applications*(88), 351-371. doi:10.1016/B978-0-08-100433-3.00013-0
- [12] Melnikova, R., Ehrmann, A., & Finsterbusch, K. (2014). 3D printing of textile-based structures by Fused Deposition Modelling (FDM) with different polymer materials. *2014 Global Conference on Polymer and Composite Materials (Pcm 2014)*, 62. doi:10.1088/1757-899x/62/1/012018
- [13] Sanatgar, R. H., Campagne, C., & Nierstrasz, V. (2017). Investigation of the adhesion properties of direct 3D printing of polymers and nanocomposites on textiles: Effect of FDM printing process parameters. *Applied Surface Science*, 403, 551-563. doi:10.1016/j.apsusc.2017.01.112

- [14] Stansbury, J. W., & Idacavage, M. J. (2016). 3D printing with polymers: Challenges among expanding options and opportunities. *Dental Materials*, 32(1), 54-64. doi:10.1016/j.dental.2015.09.018
- [15] Lee, J. Y., An, J., & Chua, C. K. (2017). Fundamentals and applications of 3D printing for novel materials. *Applied Materials Today*, 7, 120-133. doi:10.1016/j.apmt.2017.02.004
- [16] Crivello, J. V., & Reichmanis, E. (2014). Photopolymer Materials and Processes for Advanced Technologies. *Chemistry of Materials*, 26(1), 533-548. doi:10.1021/cm402262g
- [17] Mohammed, J. S. (2016). Applications of 3D Printing Technologies in Oceanography. *Methods in Oceanography*, 17, 97-117. doi:10.1016/j.mio.2016.08.001
- [18] Howell, L. L., Magleby, S. P., & Olsen, B. M. (2013). *Handbook of Compliant Mechanisms*: John Wiley & Sons Ltd.
- [19] Gao, W., Zhang, Y. B., Ramanujan, D., Ramani, K., Chen, Y., Williams, C. B., . . . Zavattieri, P. D. (2015). The status, challenges, and future of additive manufacturing in engineering. *Computer-Aided Design*, 69, 65-89. doi:10.1016/j.cad.2015.04.001
- [20] Forster, A. M. (2015). *Materials Testing Standards for Additive Manufacturing of Polymer Materials: State of the Art and Standards Applicability*: US Department of Commerce, National Institute of Standards and Technology
- [21] Pruitt, L., & Bailey, L. (1998). Factors affecting near-threshold fatigue crack propagation behavior of orthopedic grade ultra high molecular weight polyethylene. *Polymer*, 39(8-9), 1545-1553. doi:Doi 10.1016/S0032-3861(97)00448-5
- [22] Sauer, J. A., & Hara, M. (1990). Effect of Molecular Variables on Crazing and Fatigue of Polymers. *Crazing in Polymers*, 2, 69-118.
- [23] Machekposhti, D. F., Tolou, N., & Herder, J. L. (2015). A Review on Compliant Joints and Rigid-Body Constant Velocity Universal Joints Toward the Design of Compliant Homokinetic Couplings. *Journal of Mechanical Design*, 137(3). doi:10.1115/1.4029318
- [24] Lobontiu, N. (2002). *Compliant Mechanisms: Design of Flexure Hinges* (Vol. 1). Boca Raton: CRC Press.
- [25] Smith, S. T. (2000). *Flexures*. London, UK: Taylor & Francis.
- [26] Berglund, M. D., Magleby, S. P., & Howell, L. L. (2000). *Design Rules for Selecting and Designing Compliant Mechanisms for Rigid-Body Replacement Synthesis*. Paper presented at the Proceedings of the 26th Design Automation Conference, ASME DETC, Baltimore, MD.
- [27] Howell, L. L., & Midha, A. (1994). A Method for the Design of Compliant Mechanisms with Small-Length Flexural Pivots. *Journal of Mechanical Design*, 116(1), 280-290. doi:Doi 10.1115/1.2919359
- [28] Midha, A., Her, I., & Salamon, B. A. (1992). A methodology for compliant mechanisms design. Part I. Introduction and large-deflection analysis.
- [29] Howell, L. L., & Midha, A. (1995). Parametric Deflection Approximations for End-Loaded Large-Deflection Beams in Compliant Mechanisms. *Journal of Mechanical Design*, 117(1), 156-165. doi:Doi 10.1115/1.2826101
- [30] Howell, L. L., & Midha, A. (1995). *Determination of the degrees of freedom of compliant mechanisms using the pseudo-rigid-body model concept*. Paper presented at the Proc. of the Ninth World Congress on the Theory of Machines and Mechanisms, Milano, Italy.

- [31] Pei, X., Yu, J. J., Zong, G. H., & Bi, S. S. (2008). The modeling of Leaf-type Isosceles-trapezoidal Flexural pivots. *Proceedings of the Asme International Design Engineering Technical Conferences and Computers and Information in Engineering Conference 2007, Vol 8, Pts a and B*, 217-223.
- [32] Yu, J. J., Pei, X., Sun, M. L., Zhao, S. S., Bi, S. S., & Zong, G. H. (2009). A New Large-stroke Compliant Joint & Micro/Nano Positioner Design Based on Compliant Building Blocks. *Reconfigurable Mechanisms and Robots*, 428-435.
- [33] Lates, D., Casvean, M., & Moica, S. (2017). Fabrication Methods of Compliant Mechanisms. *10th International Conference Interdisciplinarity in Engineering, Inter-Eng 2016, 181*, 221-225. doi:10.1016/j.proeng.2017.02.377
- [34] Teo, T. J., Yang, G., & Chen, I. (2014). Compliant Manipulators *Handbook of Manufacturing Engineering and Technology*, 1-63.
- [35] Dechev, N., Cleghorn, W. L., & Mills, J. K. (2004). Microassembly of 3-D microstructures using a compliant, passive microgripper. *Journal of Microelectromechanical Systems*, 13(2), 176-189. doi:Doi 10.1109/Jmems.2004.825311
- [36] Vogtmann, D. E., Gupta, S. K., & Bergbreiter, S. (2011). Multi-Material Compliant Mechanisms for Mobile Millirobots. *2011 Ieee International Conference on Robotics and Automation (Icra)*.
- [37] Gouker, R. M., Gupta, S. K., Bruck, H. A., & Holzschuh, T. (2006). Manufacturing of multi-material compliant mechanisms using multi-material molding. *International Journal of Advanced Manufacturing Technology*, 30(11-12), 1049-1075. doi:10.1007/s00170-005-0152-4
- [38] Mavroidis, C., DeLaurentis, K. J., Won, J., & Alam, M. (2001). Fabrication of non-assembly mechanisms and robotic systems using rapid prototyping. *Journal of Mechanical Design*, 123(4), 516-524. doi:Doi 10.1115/1.1415034
- [39] Cali, J., Calian, D. A., Amati, C., Kleinberger, R., Steed, A., Kautz, J., & Weyrich, T. (2012). 3D-Printing of Non-Assembly, Articulated Models. *Acm Transactions on Graphics*, 31(6). doi:10.1145/2366145.2366149
- [40] De Laurentis, K. J., Kong, F. F., & Mavroidis, C. (2002). Procedure for Rapid Fabrication of Non- Assembly Mechanisms With Embedded Components. 1239-1245.
- [41] Gibson, I., Rosen, D. W., & Stucker, B. (2018). Introduction and Basic Principles. *Additive Manufacturing Technologies*, 20-35.
- [42] Crawford, R. J., & Benham, P. P. (1975). Some Fatigue Characteristics of Thermoplastics. *Polymer*, 16(12), 908-914. doi:Doi 10.1016/0032-3861(75)90212-8
- [43] Hertzberg, R. W., Vinci, R. P., & Hertzberg, J. L. (2012). *Deformation and Fracture Mechanics of Engineering Materials*: Wiley.
- [44] Constable, I., Williams, J. G., & Burns, D. J. (1970). Fatigue and Cyclic Thermal Softening of Thermoplastics. *Journal of Mechanical Engineering Science*, 12(1), 20-29.
- [45] Crawford, R. J., & Benham, P. P. (1974). Cyclic Stress Fatigue and Thermal Softening Failure of a Thermoplastic. *Journal of Materials Science*, 9(1), 18-28. doi:Doi 10.1007/Bf00554752
- [46] Essman, U., Gösele, U., & Mughrabi, H. (1981). A Model of Extrusions and Intrusions in Fatigued Metals I. Point-Defect Production and the Growth of Extrusions. *Philosophical Magazine*, 44(2), 405-426.
- [47] Schijve, J. (2003). Fatigue of structures and materials in the 20th century and the

- state of the art. *International Journal of Fatigue*, 25(8), 679-702. doi:10.1016/S0142-1123(03)00051-3
- [48] Chowdhury, P., & Sehitoglu, H. (2016). Mechanisms of fatigue crack growth - a critical digest of theoretical developments. *Fatigue & Fracture of Engineering Materials & Structures*, 39(6), 652-674. doi:10.1111/ffe.12392
- [49] Lin, M. R., Fine, M. E., & Mura, T. (1986). Fatigue Crack Initiation on Slip Bands - Theory and Experiment. *Acta Metallurgica*, 34(4), 619-628. doi:10.1016/0001-6160(86)90177-X
- [50] Taylor, D., & Knott, J. F. (1981). Fatigue Crack-Propagation Behavior of Short Cracks - the Effect of Microstructure. *Fatigue of Engineering Materials and Structures*, 4(2), 147-155. doi:10.1111/j.1460-2695.1981.tb01116.x
- [51] Zurek, A. K., James, M. R., & Morris, W. L. (1983). The Effect of Grain-Size on Fatigue Growth of Short Cracks. *Metallurgical Transactions a-Physical Metallurgy and Materials Science*, 14(8), 1697-1705. doi:10.1007/Bf02654397
- [52] Schultz, J. M. (1977). Fatigue Behavior of Engineering Polymers. *Treatise on Materials Science and Technology*, 10, 599-636.
- [53] Ang, K. C., Leong, K. F., Chua, C. K., & Chandrasekaran, M. (2006). Investigation of the mechanical properties and porosity relationships in fused deposition modelling-fabricated porous structures. *Rapid Prototyping Journal*, 12(2), 100-105. doi:10.1108/135525406106524471
- [54] Equbal, A., Sood, A. K., & Mahapatra, S. S. (2010). Prediction of Dimensional Accuracy in Fused Deposition Modelling: a Fuzzy Logic Approach. *International Journal of Productivity and Quality Management*, 7(1), 22-43.
- [55] Sood, A. K., Ohdar, R. K., & Mahapatra, S. S. (2010). Parametric appraisal of mechanical property of fused deposition modelling processed parts. *Materials & Design*, 31(1), 287-295. doi:10.1016/j.matdes.2009.06.016
- [56] Sood, A. K., Ohdar, R. K., & Mahapatra, S. S. (2012). Experimental Investigation and Empirical Modelling of FDM Process for Compressive Strength Improvement. *Journal of Advanced Research*, 3(1), 81-90.
- [57] Zarringhalam, H., Hopkinson, N., Kamperman, N. F., & de Vlieger, J. J. (2006). Effects of processing on microstructure and properties of SLS Nylon 12. *Materials Science and Engineering a-Structural Materials Properties Microstructure and Processing*, 435, 172-180. doi:10.1016/j.msea.2006.07.084
- [58] Molai, R., & Fatemi, A. (2018). Fatigue Design with Additive Manufactured Metals: Issues to Consider and Perspective for Future Research. *Procedia Engineering*, 213, 5-16.
- [59] (2017). *ASTM D7791-12 Standard Test Method for Uniaxial Fatigue Properties of Plastics*. West Conshohocken, PA: ASTM International.
- [60] (2012). *ASTM D3479/D3479M-12 Standard Test Method for Tension-Tension Fatigue of Polymer Matrix Composite Materials*. West Conshohocken, PA: ASTM International
- [61] (2017). *ASTM D7774-17 Standard Test Method for Flexural Fatigue Properties of Plastics*. West Conshohocken, PA: ASTM International
- [62] (2003). *ISO 13003:2003 Fibre-reinforced plastics -- Determination of fatigue properties under cyclic loading conditions*. Switzerland: ISO.
- [63] (2011). *ASTM D6115-97(2011) Standard Test Method for Mode I Fatigue Delamination Growth Onset of Unidirectional Fiber-Reinforced Polymer Matrix Composites*. West Conshohocken, PA: ASTM International

- [64] (2014). *ISO 15850:2014 Plastics -- Determination of tension-tension fatigue crack propagation -- Linear elastic fracture mechanics (LEFM) approach*. Switzerland ISO.
- [65] Ombregt, L. (2013). Applied anatomy of the wrist, thumb and hand *A System of Orthopaedic Medicine* (pp. e102-e111): Churchill Livingstone.
- [66] Hume, M. C., Gellman, H., McKellop, H., & Brumfield, R. H., Jr. (1990). Functional range of motion of the joints of the hand. *J Hand Surg Am*, 15(2), 240-243.
- [67] Gracia-Ibanez, V., Vergara, M., Sancho-Bru, J. L., Mora, M. C., & Piqueras, C. (2017). Functional range of motion of the hand joints in activities of the International Classification of Functioning, Disability and Health. *J Hand Ther*, 30(3), 337-347. doi:10.1016/j.jht.2016.08.001
- [68] Pham, H. T., Pathirana, P. N., & Caelli, T. (2014). Functional range of movement of the hand: declination angles to reachable space. *Conf Proc IEEE Eng Med Biol Soc*, 2014, 6230-6233. doi:10.1109/EMBC.2014.6945052
- [69] Dandekar, K., Raju, B. I., & Srinivasan, M. A. (2003). 3-D finite-element models of human and monkey fingertips to investigate the mechanics of tactile sense. *J Biomech Eng*, 125(5), 682-691.
- [70] Chandran, K. R. (2016). Mechanical Fatigue of Polymers: A New Approach to Characterize the SN Behavior on the Basis of Macroscopic Crack Growth Mechanism. *Polymer*, 91, 222-238.
- [71] Tielen, V., & Bellouard, Y. (2014). Three-Dimensional Glass Monolithic Micro-Flexure Fabricated by Femtosecond Laser Exposure and Chemical Etching. *Micromachines*, 5(3), 697-710. doi:10.3390/mi5030697
- [72] B.V., U. (2018). Ultimaker 3 Specification Sheet.
- [73] B.V., U. (2017). Technical Data Sheet Nylon.
- [74] B.V., U. (2017). Technical Data Sheet PLA.
- [75] B.V., U. (2017). Technical Data Sheet ABS.
- [76] B.V., U. (2017). Technical Data Sheet TPU 95A.
- [77] B.V., U. (2017). Technical Data Sheet Tough PLA.
- [78] B.V., U. (2017). Technical Data Sheet CPE.
- [79] B.V., U. (2017). Technical Data Sheet CPE+.
- [80] B.V., U. (2017). Technical Data Sheet PP.
- [81] Stratasys. (2015). PC (Polycarbonate) Production Grade Thermoplastic for Fortus 3D Production Systems.
- [82] Gomez, J. F., Booker, J. D., & Mellor, P. H. (2015). Stress optimization of leaf-spring crossed flexure pivots for an active Gurney flap mechanism. *Industrial and Commercial Applications of Smart Structures Technologies 2015*, 9433. doi:10.1117/12.2082890
- [83] Jensen, B. D., & Howell, L. L. (2002). The modeling of cross-axis flexural pivots. *Mechanism and Machine Theory*, 37(5), 461-476. doi:10.1016/S0094-114x(02)00007-1
- [84] Cantrell, J. T., Rohde, S., Damiani, D., Gurnani, R., DiSandro, L., Anton, J., . . . Ifju, P. G. (2017). Experimental characterization of the mechanical properties of 3D-printed ABS and polycarbonate parts. *Rapid Prototyping Journal*, 23(4), 811-824. doi:10.1108/Rpj-03-2016-0042
- [85] Zou, R., Xia, Y., Liu, S. Y., Hu, P., Hou, W. B., Hu, Q. Y., & Shan, C. L.

- (2016). Isotropic and anisotropic elasticity and yielding of 3D printed material. *Composites Part B-Engineering*, 99, 506-513. doi:10.1016/j.compositesb.2016.06.009
- [86] Berselli, G., Piccinini, M., & Vassura, G. (2011). Comparative Evaluation of the Selective Compliance in Elastic Joints for Robotic Structures. *2011 Ieee International Conference on Robotics and Automation (Icra)*.
- [87] Jeanneau, A., Herder, J. L., Laliberté, T., & Gosselin, C. (2004). *A Compliant Rolling Contact Joint and Its Application in a 3-DOF Planar Parallel Mechanism With Kinematic Analysis*. Paper presented at the ASME 2004 Design Engineering Technical Conferences and Computers and Information in Engineering Conference.
- [88] Cannon, J. R., Lusk, C. P., & Howell, L. L. (2005). Compliant rolling-contact element mechanisms. *Proceedings of the ASME International Design Engineering Technical Conferences and Computers and Information in Engineering Conference, Vol 7, Pts A and B*, 3-13.
- [89] Kim, Y., Lee, J., & Park, J. (2013). Compliant Joint Actuator With Dual Spiral Springs. *Ieee-Asme Transactions on Mechatronics*, 18(6), 1839-1844. doi:10.1109/Tmech.2013.2260554
- [90] Mechanical Springs. (1963) *Machine Tool Design Handbook* (pp. 143-154): Tata McGraw-Hill
- [91] Luchetti, M., Cutti, A. G., Verni, G., Sacchetti, R., & Rossi, N. (2015). Impact of Michelangelo prosthetic hand: Findings from a crossover longitudinal study. *Journal of Rehabilitation Research and Development*, 52(5), 605-618. doi:10.1682/Jrrd.2014.11.0283
- [92] Lee, J., & Huang, A. (2013). Fatigue analysis of FDM materials. *Rapid Prototyping Journal*, 19(4), 291-299. doi:10.1108/13552541311323290
- [93] Zhang, H. Y., Cai, L. L., Golub, M., Zhang, Y., Yang, X. H., Schlarman, K., & Zhang, J. (2018). Tensile, Creep, and Fatigue Behaviors of 3D-Printed Acrylonitrile Butadiene Styrene. *Journal of Materials Engineering and Performance*, 27(1), 57-62. doi:10.1007/s11665-017-2961-7
- [94] Ziemian, S., Okwara, M., & Ziemian, C. W. (2015). Tensile and fatigue behavior of layered acrylonitrile butadiene styrene. *Rapid Prototyping Journal*, 21(3), 270-278. doi:10.1108/Rpj-09-2013-0086
- [95] Ziemian, C. W., Ziemian, R. D., & Haile, K. V. (2016). Characterization of stiffness degradation caused by fatigue damage of additive manufactured parts. *Materials & Design*, 109, 209-218. doi:10.1016/j.matdes.2016.07.080
- [96] Van Hooreweder, B., De Coninck, F., Moens, D., Boonen, R., & Sas, P. (2010). Microstructural characterization of SLS-PA12 specimens under dynamic tension/compression excitation. *Polymer Testing*, 29(3), 319-326. doi:10.1016/j.polymertesting.2009.12.006
- [97] Munguia, J., & Dalgarno, K. (2015). Fatigue behaviour of laser sintered Nylon 12 in rotating and reversed bending tests. *Materials Science and Technology*, 31(8), 904-911. doi:10.1179/1743284715y.0000000014
- [98] Munguia, J., & Dalgarno, K. (2014). Fatigue behaviour of laser-sintered PA12 specimens under four-point rotating bending. *Rapid Prototyping Journal*, 20(4), 291-300. doi:10.1108/Rpj-07-2012-0064
- [99] Van Hooreweder, B., Moens, D., Boonen, R., Kruth, J. P., & Sas, P. (2013). On the difference in material structure and fatigue properties of nylon specimens produced by injection molding and selective laser sintering. *Polymer Testing*, 32(5), 972-981. doi:10.1016/j.polymertesting.2013.04.014

- [100] Van Hooreweder, B., & Kruth, J. P. (2014). High cycle fatigue properties of selective laser sintered parts in polyamide 12. *Cirp Annals-Manufacturing Technology*, 63(1), 241-244. doi:10.1016/j.cirp.2014.03.060

7 Appendix

A Initial Matlab Codes

A.1 Cross axis hinge plot of stress against deflection angle

```
%CAH_Stress

clear all
close all

E1=579;
E2=2030;

theta=0:0.1:1.5708;

t=0.5;
r=20;
n=1;

S1=0.189393+0.899845*n-0.4333*n^2+0.097866*n^3-0.00839*n^4;
S2=-0.09799+0.982995*n-0.96184*n^2+0.413319*n^3-
0.08387*n^4+0.006530*n^5;

Sy_1=ones(length(theta))*27.8;
Sy_2=ones(length(theta))*43.6;

Stress_1=E1*t/(2*r)*(S1*theta+S2*theta.^2);
Stress_2=E2*t/(2*r)*(S1*theta+S2*theta.^2);

figure

plot(theta,Stress_1, theta, Sy_1)
xlabel('Deflection (rad)')
ylabel('Stess (MPa)')
title('Stress vs. Deflection for Nylon')

figure

plot(theta,Stress_2, theta, Sy_2)
xlabel('Deflection (rad)')
ylabel('Stess (MPa)')
title('Stress vs. Deflection for ABS')
```

A.2 Contact bearing plot of stress against the radius of curvature

```
%CB_Stress

clear all
close all

Rs=1:1:10;
Ro=Rs+1+0.75/2;
t=0.75;
```

```

Sy_1=ones(length(Rs))*27.8;
Sy_2=ones(length(Rs))*43.6;

E1=579;
E2=2030;

Re=(1./Rs-1./Ro).^-1;

stress1=E1*t./(2*Re);
stress2=E2*t./(2*Re);

figure

plot(Rs, stress1, Rs, Sy_1)
xlabel('Radius of Curvature of Constraining Surface (mm)')
ylabel('Stress (MPa)')
title('Stress vs. Radius of Curvature for Nylon')

figure

plot(Rs, stress2, Rs, Sy_2)
xlabel('Radius of Curvature of Constraining Surface (mm)')
ylabel('Stress (MPa)')
title('Stress vs. Radius of Curvature for ABS')

```

A.3 Spiral plot of stress against the thickness

```

%Spiral_Stress_1

clear all
close all

alpha=90;
a=[0.92,1.25,1.75,2.24];
Ri=[1.63,2.12,1.81,1.67];
Re=[6.90,7.99,8.24,8.49];
t=[1.85,1.50,1.00,0.50];

Sy_1=ones(length(a))*27.8;
Sy_2=ones(length(a))*43.6;

E1=579;
E2=2030;

stress1=(alpha*E1*t.*(a+t)./(360*(Re.^2-Ri.^2)));
stress2=(alpha*E2*t.*(a+t)./(360*(Re.^2-Ri.^2)));

figure

plot(t, stress1, t, Sy_1)
xlabel('Thickness (mm)')
ylabel('Stress (MPa)')
title('Stress vs. Thickness for Nylon')

figure

plot(t, stress2, t, Sy_2)
xlabel('Thickness (mm)')

```

```
ylabel('Stess (MPa)')
title('Stress vs. Thickness for ABS')
```

A.4 Spiral plot of stress against the deflection angle

```
%Spiral_Stress_2

clear all
close all

alpha=0:5:90;
a=2.24;
Ri=1.67;
Re=8.49;
t=0.50;

Sy_1=ones(length(alpha))*27.8;
Sy_2=ones(length(alpha))*43.6;

E1=579;
E2=2030;

stress1=alpha.*E1*t*(a+t)/(360*(Re^2-Ri^2));
stress2=alpha.*E2*t*(a+t)/(360*(Re^2-Ri^2));

figure

plot(alpha, stress1, alpha, Sy_1)
xlabel('Deflection (deg)')
ylabel('Stess (MPa)')
title('Stress vs. Deflection for Nylon')

figure

plot(alpha, stress2, alpha, Sy_2)
xlabel('Deflection (deg)')
ylabel('Stess (MPa)')
title('Stress vs. Deflection for ABS')
```

B Technical Drawings

Base

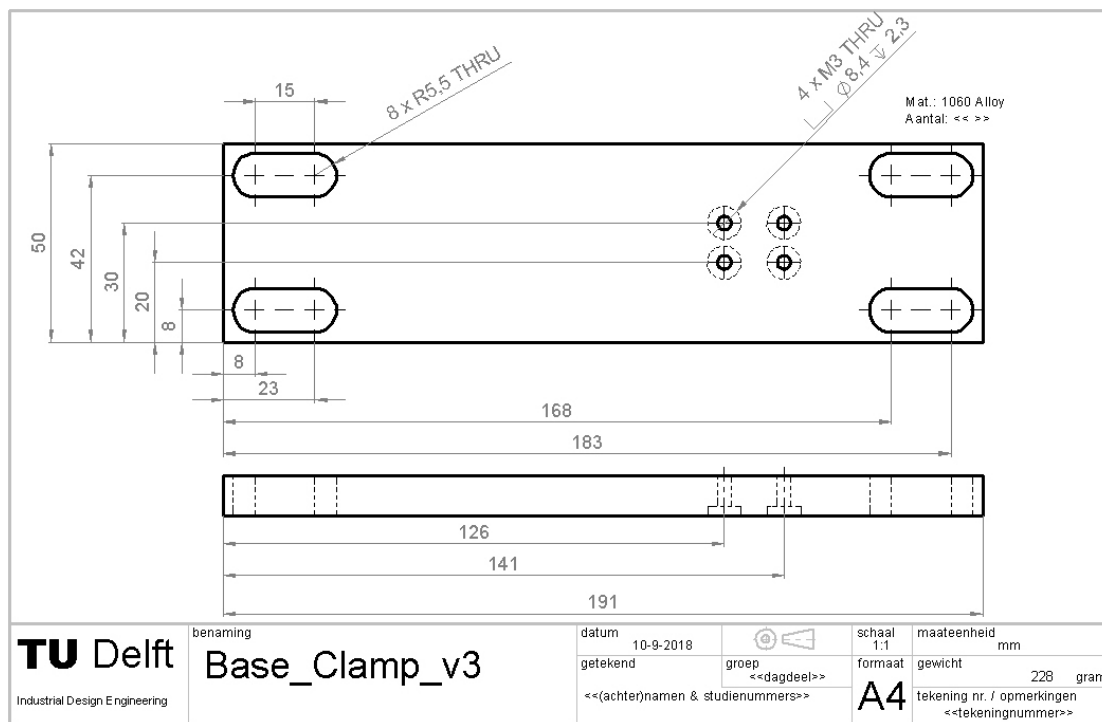


Figure 36. The technical drawing of the base that connects the clamping stand to the Instron.

Tower

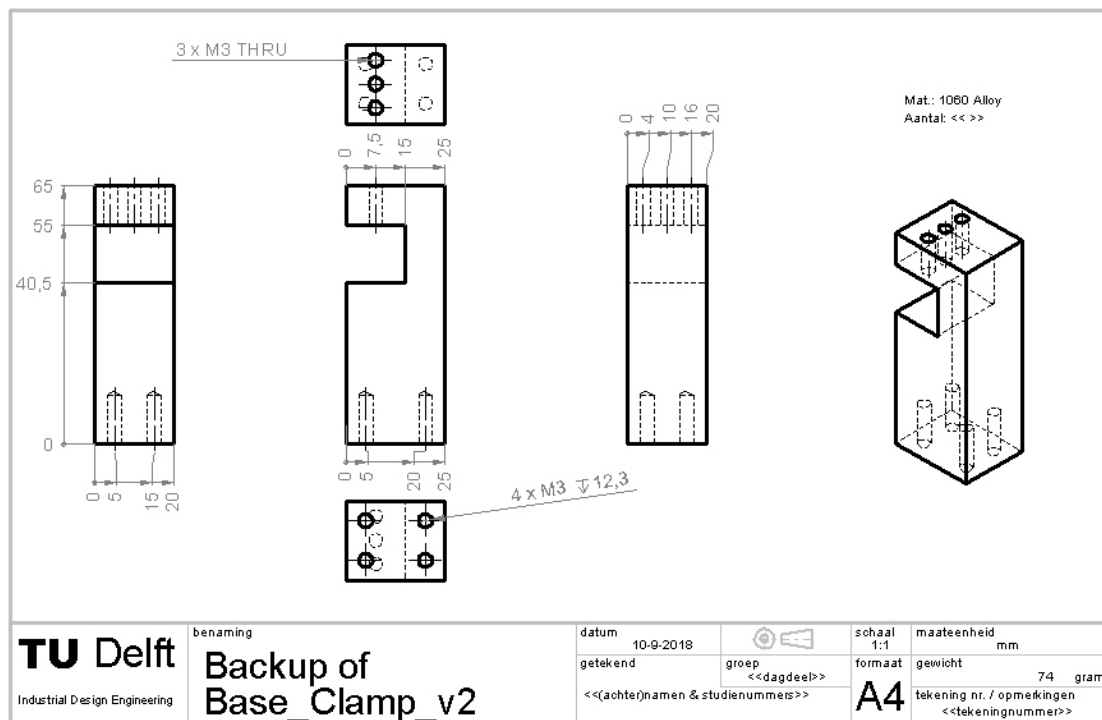


Figure 37. The technical drawing of the clamping tower, which connects the base and holds the specimens in place.

Press

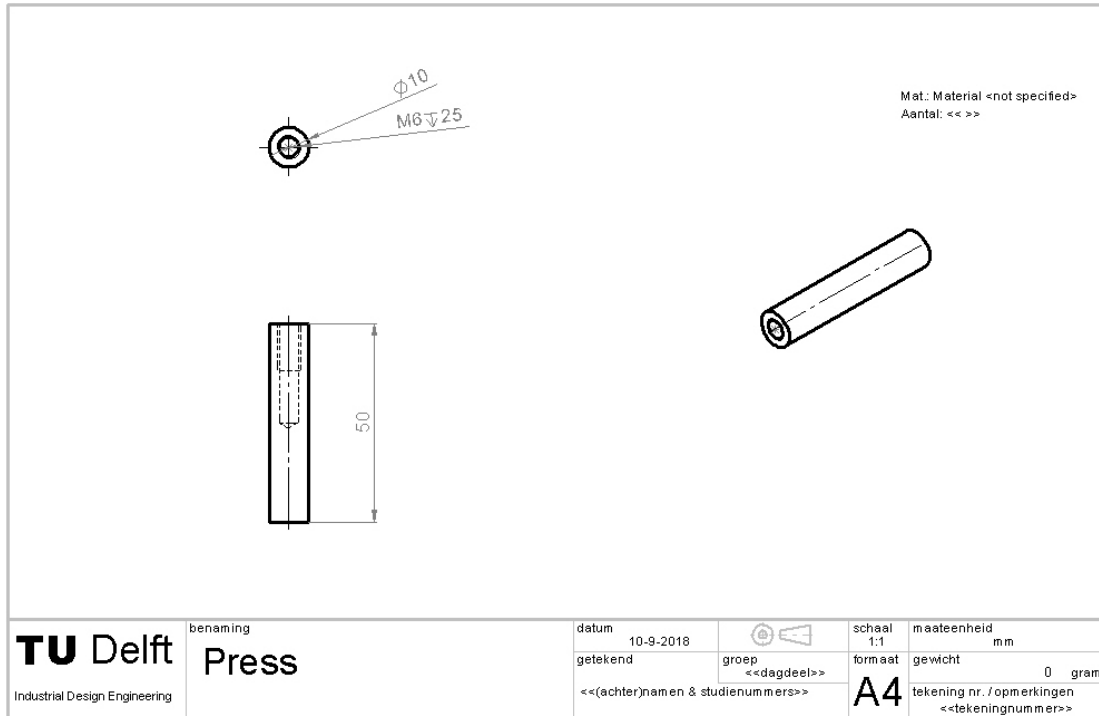


Figure 38. The technical drawing of the press, which connects to the Instron and deflects the specimen to ninety degrees.

C First Iteration Pictures

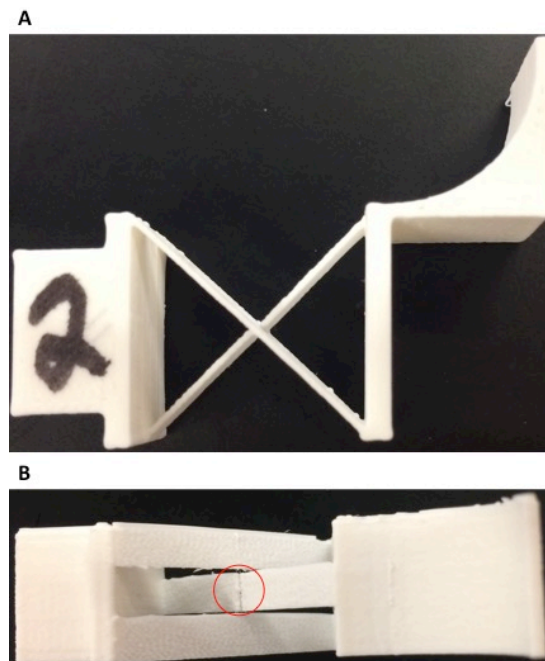


Figure 39. The first cross axis hinge made of ABS which was fatigue tested. After fatigue testing, A) the front view and B) top view can be seen. In the top view, it can be seen that there was one fracture in the center of the middle flexural arm.

D Second Iteration Pictures

D.1 Cross axis hinge

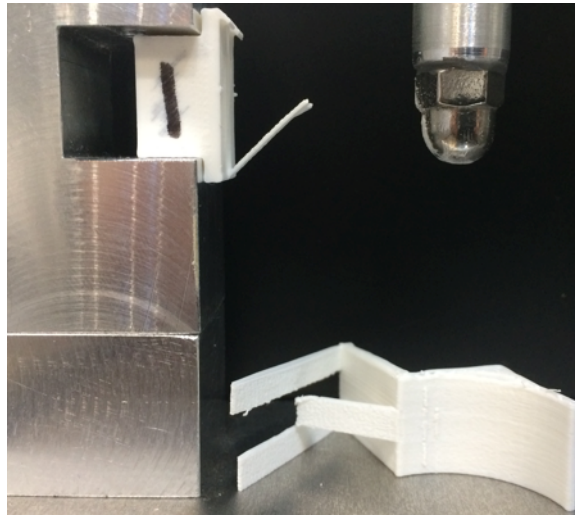


Figure 40. The second cross axis hinge made of ABS that was fatigue tested. The specimen fractured in several locations, breaking the specimen into two parts.

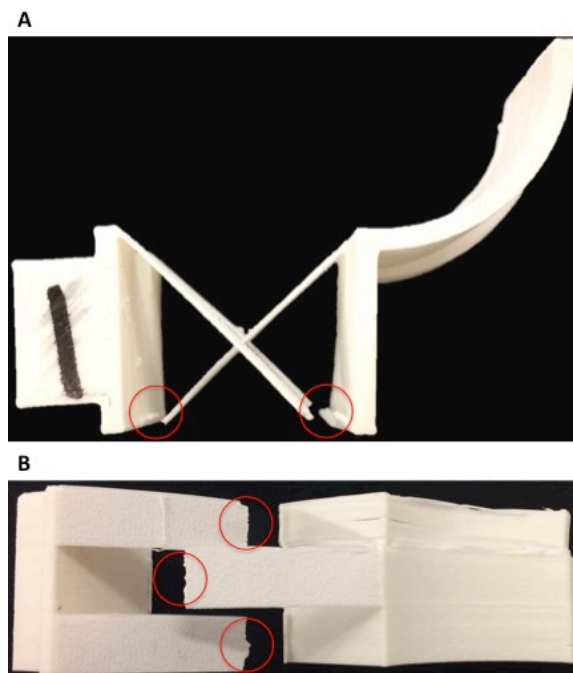


Figure 41. The second cross axis hinge, 8mm width, made of ABS that was fatigue tested. After fatigue testing, A) the front view and B) top view can be seen. In the top view, it can be seen that there were three fractures, which one fracture in each flexural arm.

D.2 Spiral

Test 1

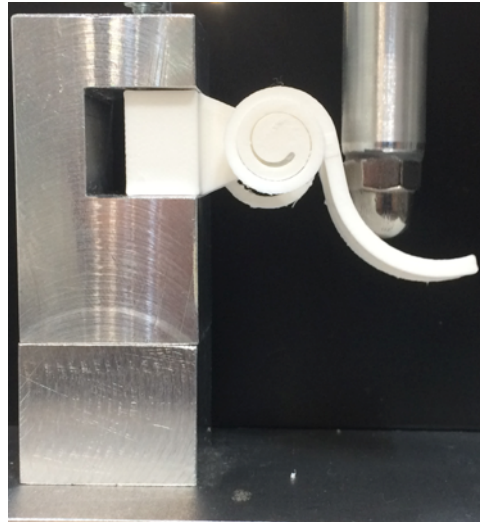


Figure 42. The second spiral design is seen during fatigue testing, where the Instron has almost deflected the first specimen to the maximum deflection of ninety degrees.

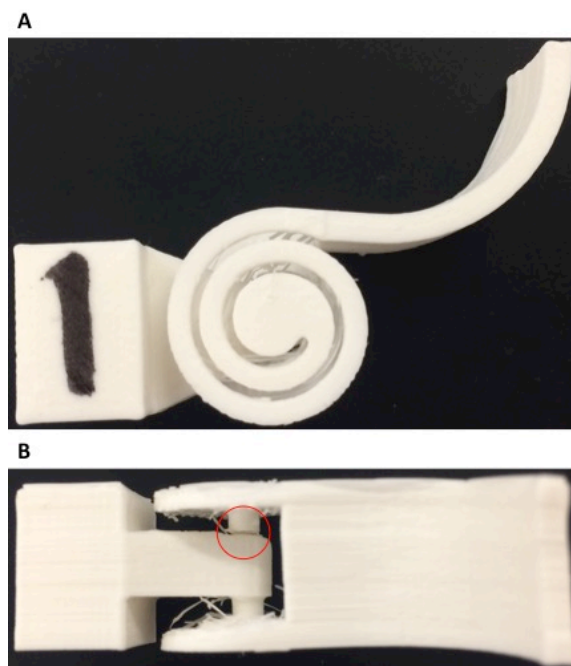


Figure 43. The second spiral design made of ABS that was fatigue tested. After fatigue testing, A) the front view and B) top view can be seen. In the top view, it can be seen that there was one fracture between the axle and base.

Test 2

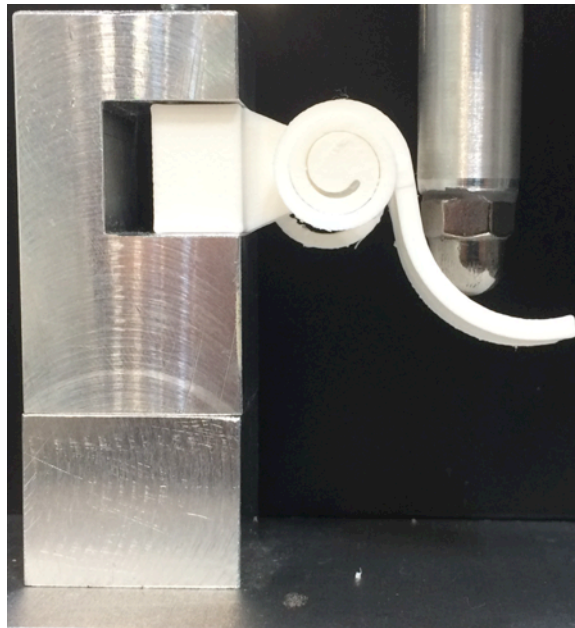


Figure 44. The second spiral design is seen during fatigue testing, where the Instron has almost deflected the second specimen to the maximum deflection of ninety degrees.

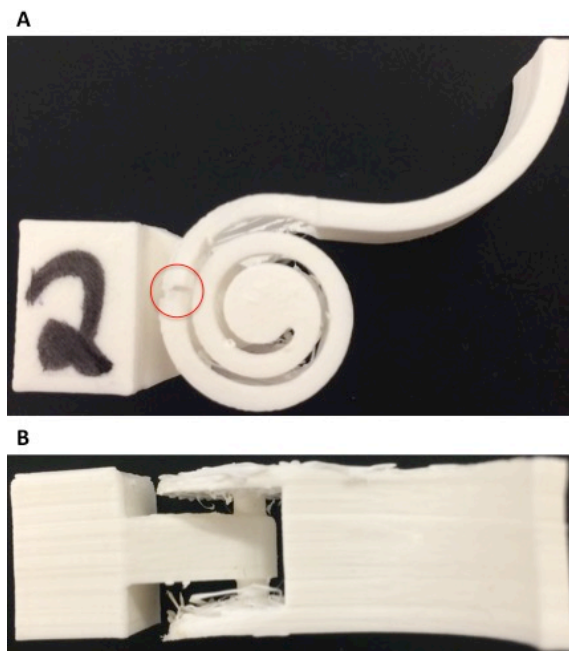


Figure 45. The second spiral design made of ABS that was fatigue tested. After fatigue testing, A) the front view and B) top view can be seen. In the front view, it can be seen that there was one fracture in the outer spiral on the left side.

Test 3

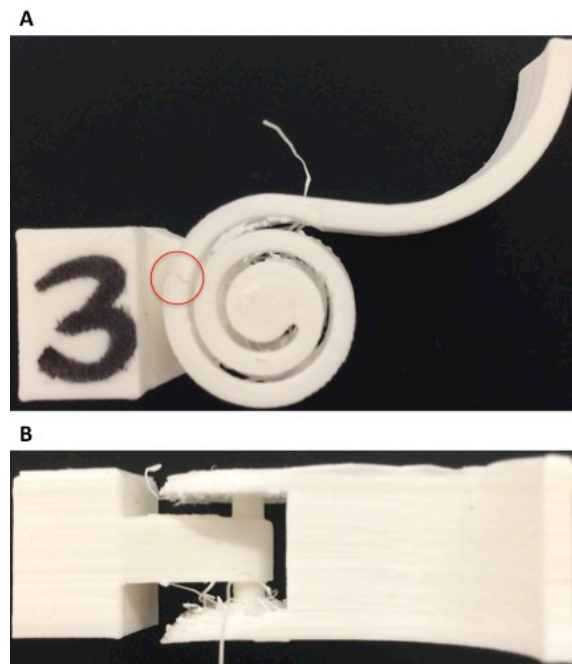


Figure 46. The second spiral design made of ABS that was fatigue tested. After fatigue testing, A) the front view and B) top view can be seen. In the front view, it can be seen that there was one fracture in the outer spiral on the left side.

E Cross Axis Hinge Abaqus Stress Distribution

ABS

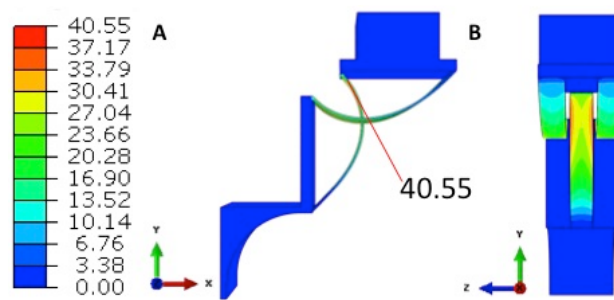


Figure 47. With a deflection of ninety degrees, the cross axis hinge has a maximum von Mises stress of 40.55 MPa in ABS. The stress distribution can be seen in A) the front view and B) top view.

Nylon

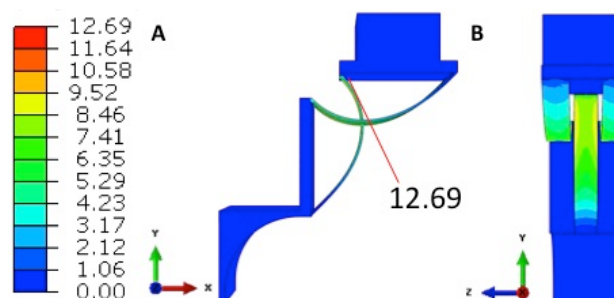


Figure 48. With a deflection of ninety degrees, the cross axis hinge has a maximum von Mises stress of 12.69 MPa in nylon. The stress distribution can be seen in A) the front view and B) top view.

F Cross Axis Hinge Fatigue Result Pictures

ABS sample 1

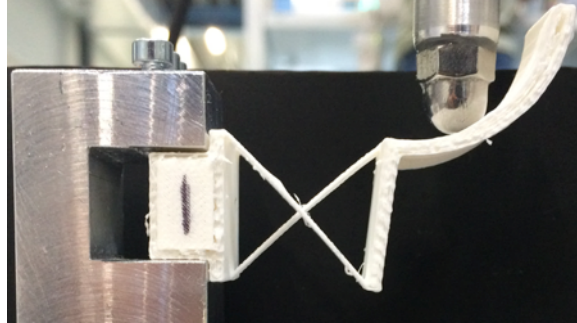


Figure 49. The first of the final three specimens for the cross axis hinge in ABS is shown. The specimen is shown during testing, with the specimen only deflected a few degrees.

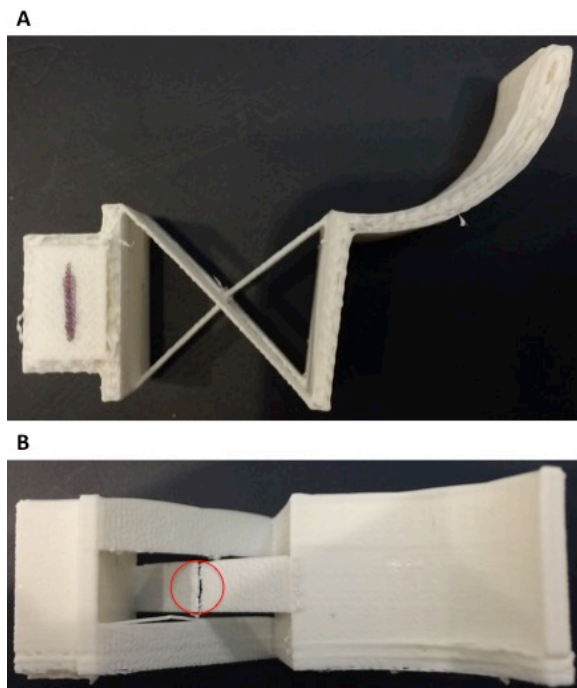


Figure 50. The first of the final three specimens that was fatigue tested for the cross axis hinge in ABS. After fatigue testing, A) the front view and B) top view can be seen. In the top view, it can be seen that there was one fracture located in the center of the middle flexural arm.

ABS sample 2

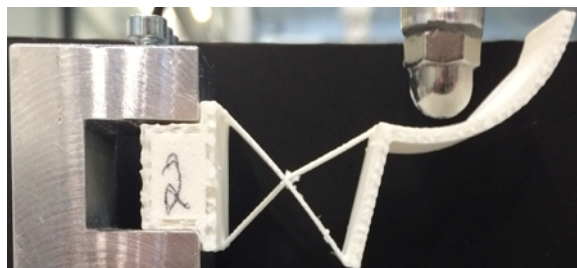


Figure 51. The second of the final three specimens for the cross axis hinge in ABS is shown. The specimen is shown during testing, with the specimen only deflected a few degrees.

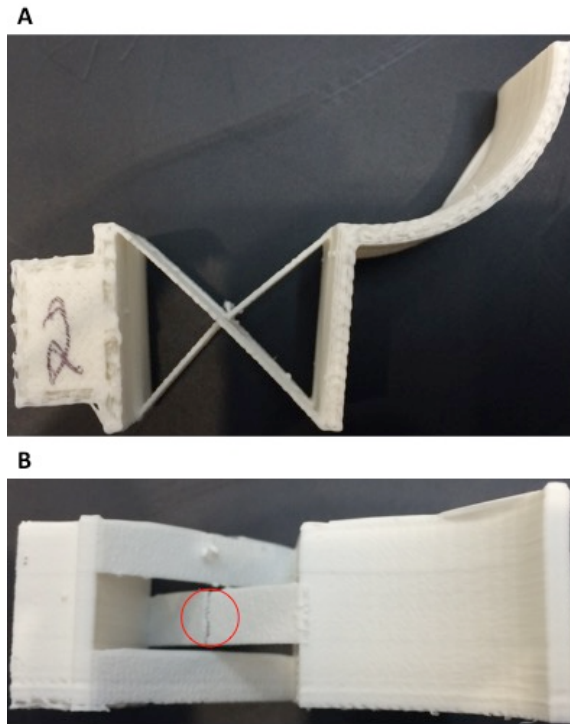


Figure 52. The second of the final three specimens that was fatigue tested for the cross axis hinge in ABS. After fatigue testing, A) the front view and B) top view can be seen. In the top view, it can be seen that there was one fracture located in the center of the middle flexural arm.

ABS sample 3

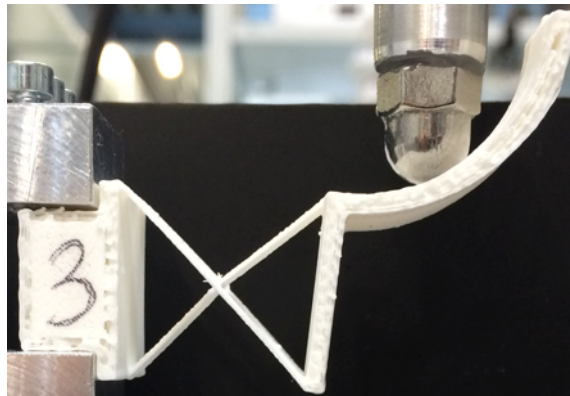


Figure 53. The third of the final three specimens for the cross axis hinge in ABS is shown. The specimen is shown during testing, with the specimen only deflected a few degrees.

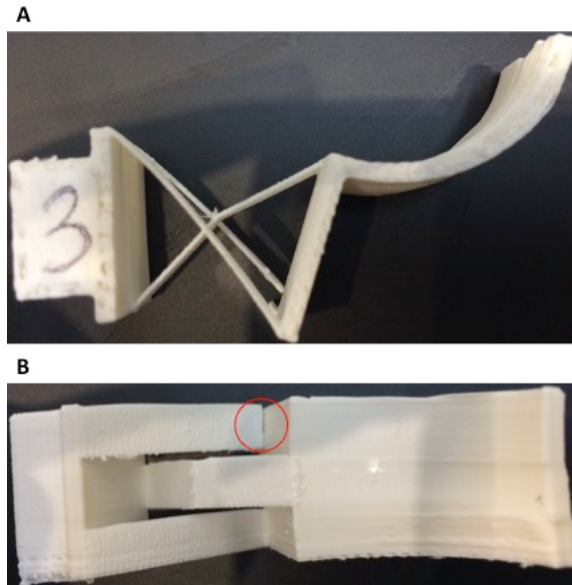


Figure 54. The third of the final three specimens that was fatigue tested for the cross axis hinge in ABS. After fatigue testing, A) the front view and B) top view can be seen. In the top view, it can be seen that there was one fracture located at the connection between the flexural arm and the base in the left flexural arm.

Nylon sample 1

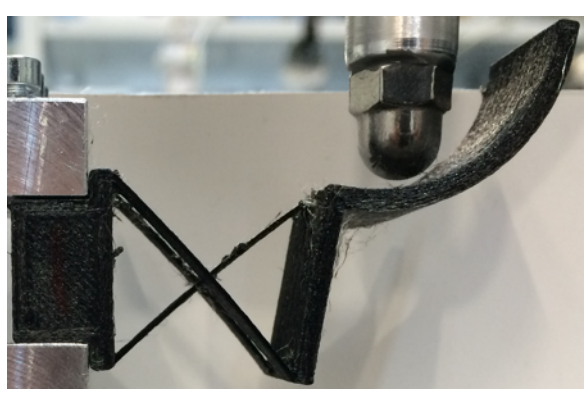


Figure 55. The first of the final three specimens for the cross axis hinge in nylon is shown. The specimen is shown during testing, where the specimen is deflected a few degrees from its original position due to creep.

Nylon sample 2

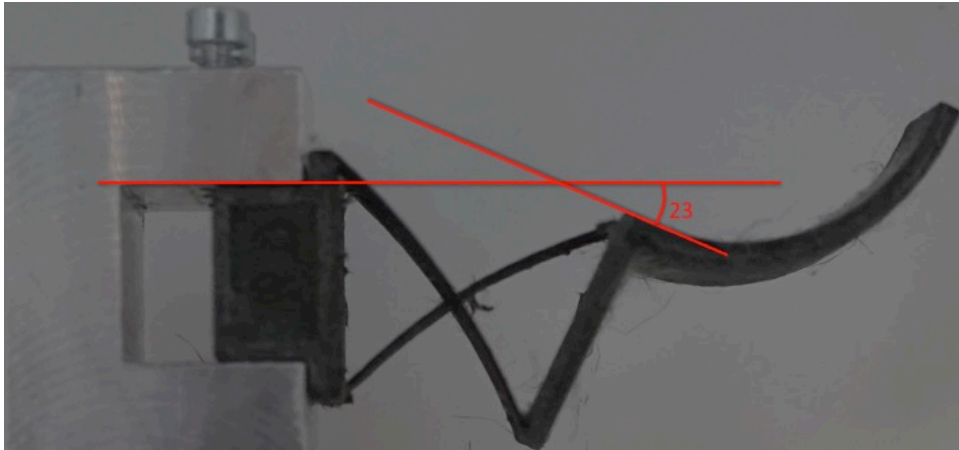


Figure 56. The front view of the second cross axis hinge sample, after fatigue testing, being held in the clamping stand. The sample was unable to return to its original position by an angle of twenty-three degrees.

Nylon sample 3

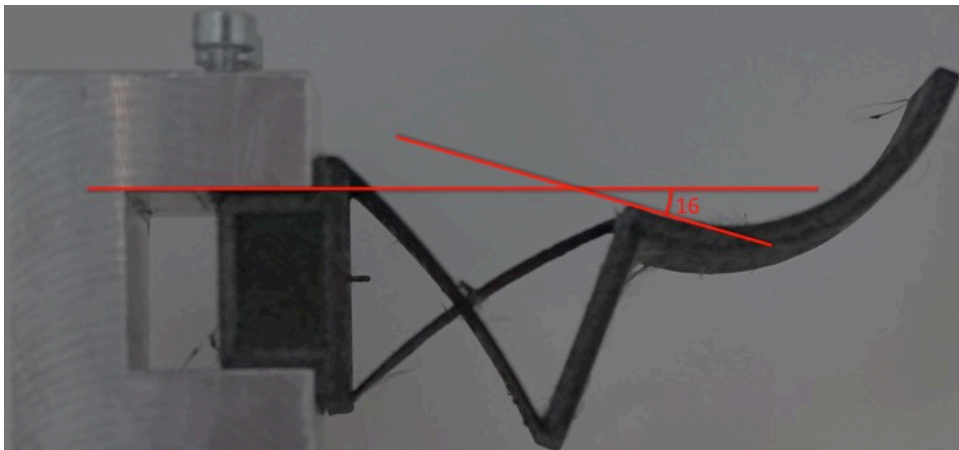


Figure 57. The front view of the second cross axis hinge sample, after fatigue testing, being held in the clamping stand. The sample was unable to return to its original position by an angle of sixteen degrees.

G New Spiral Matlab Code

```
%Spiral Stress 1.5mm  
  
clear all  
close all  
  
alpha=0:5:90;  
a=1.7;  
Ri=1.21;  
Re=7.99;  
t=1.50;  
  
Sy_1=ones(length(alpha))*27.8;  
Sy_2=ones(length(alpha))*43.6;  
  
E1=579;  
E2=2030;
```

```
stress1=(alpha.*E1*t*(a+t))/(360*(Re^2-Ri^2));  
stress2=(alpha.*E2*t*(a+t))/(360*(Re^2-Ri^2));
```

figure

```
plot(alpha, stress1, alpha, Sy_1)  
xlabel('Deflection (deg)')  
ylabel('Stess (MPa)')  
title('Stress vs. Deflection for Nylon')
```

figure

```
plot(alpha, stress2, alpha, Sy_2)  
xlabel('Deflection (deg)')  
ylabel('Stess (MPa)')  
title('Stress vs. Deflection for ABS')
```

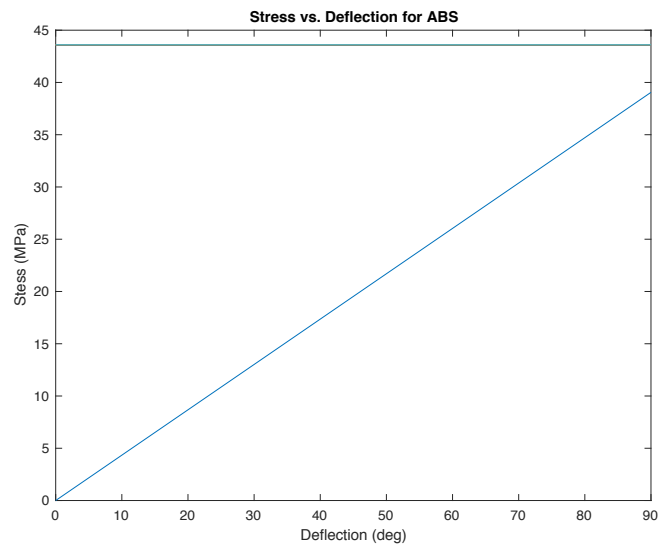


Figure 58. This plot shows the maximum stress of the ABS spiral as a function of the deflection angle from zero to ninety degrees.

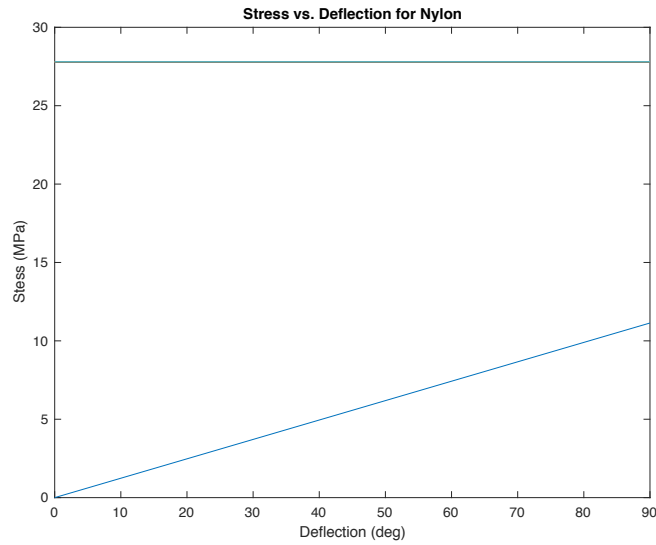


Figure 59. This plot shows the maximum stress of the nylon spiral as a function of the deflection angle from zero to ninety degrees.

H Spiral Abaqus Stress Distribution

ABS

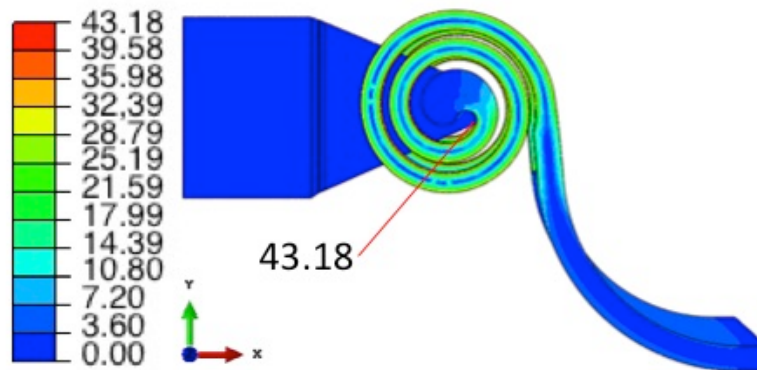


Figure 60. With a deflection of ninety degrees, the cross axis hinge has a maximum von Mises stress of 40.55 MPa in ABS. The stress distribution can be seen in A) the front view and B) top view.

Nylon

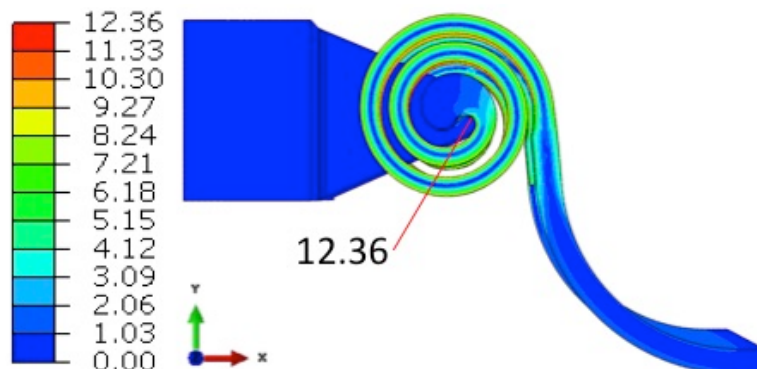


Figure 61. With a deflection of ninety degrees, the cross axis hinge has a maximum von Mises stress of 40.55 MPa in ABS. The stress distribution can be seen in A) the front view and B) top view.

I Spiral Fatigue Result Pictures

ABS sample 2

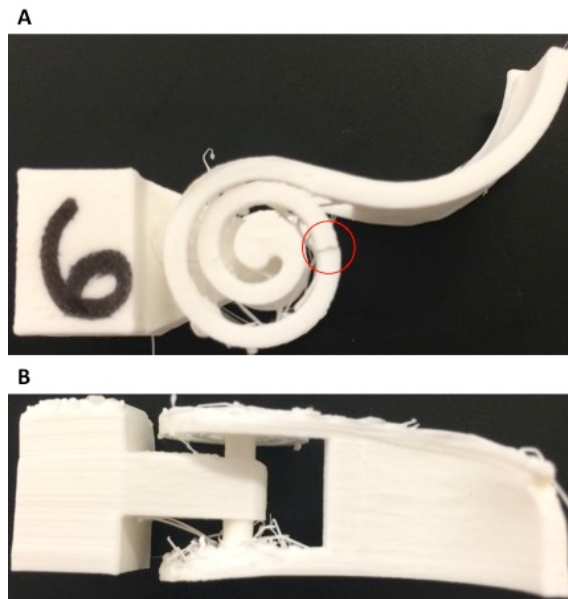


Figure 62. The second of the final three specimens that was fatigue tested for the spiral in ABS. After fatigue testing, A) the front view and B) top view can be seen. In the front view, it can be seen that there was one fracture located in the outer spiral on the right side.

ABS sample 3

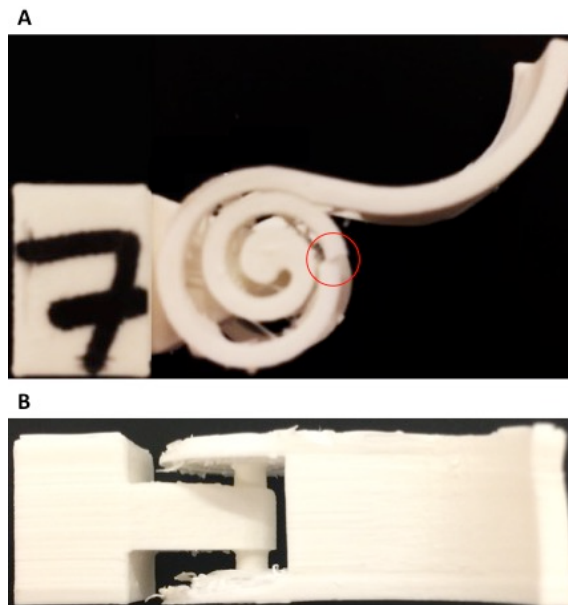


Figure 63. The third of the final three specimens that was fatigue tested for the spiral in ABS. After fatigue testing, A) the front view and B) top view can be seen. In the front view, it can be seen that there was one fracture located in the outer spiral on the right side.

Nylon sample 1

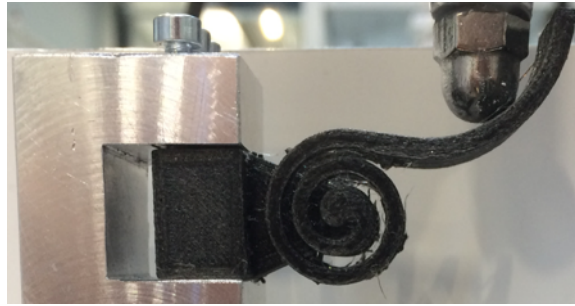


Figure 64. The first of the final three specimens for the spiral in nylon is shown. The specimen is shown during testing, where the specimen is being deflected down by the press.

Nylon sample 2

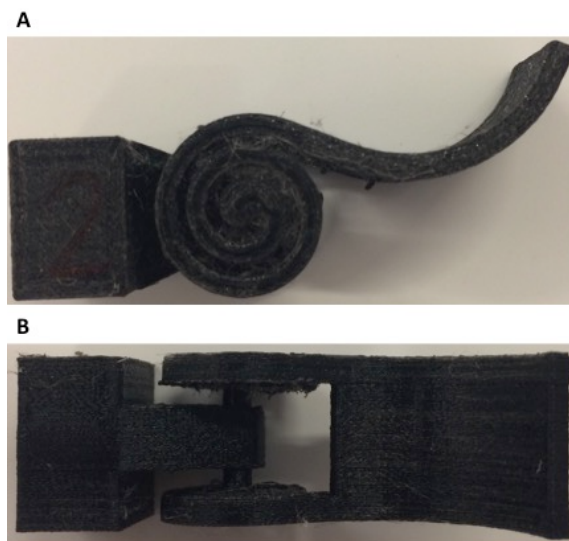


Figure 65. The second spiral design made of nylon that was fatigue tested. After fatigue testing, A) the front view and B) top view can be seen. In the both views, it can be seen that there were no fractures.

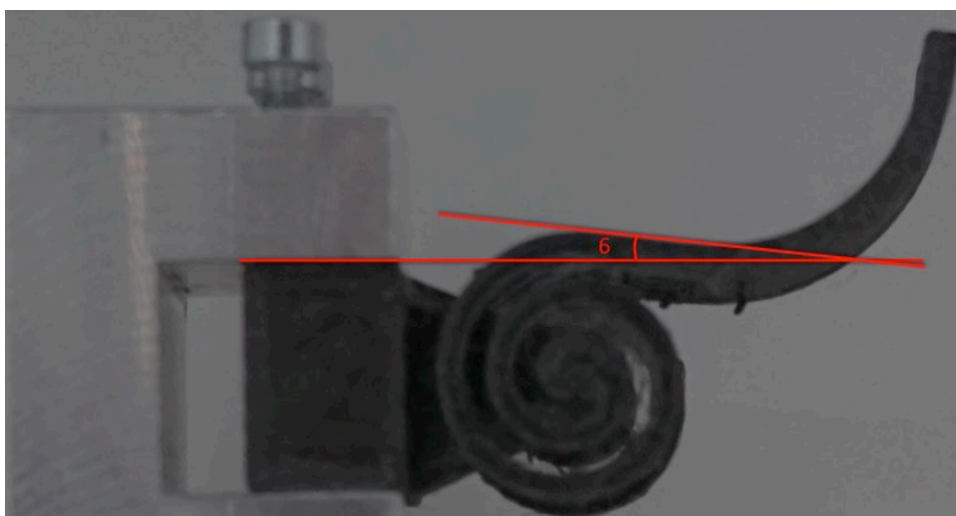


Figure 66. The front view of the second spiral sample, after fatigue testing, being held in the clamping stand. The sample was unable to return to its original position by an angle of six degrees.

Nylon sample 3

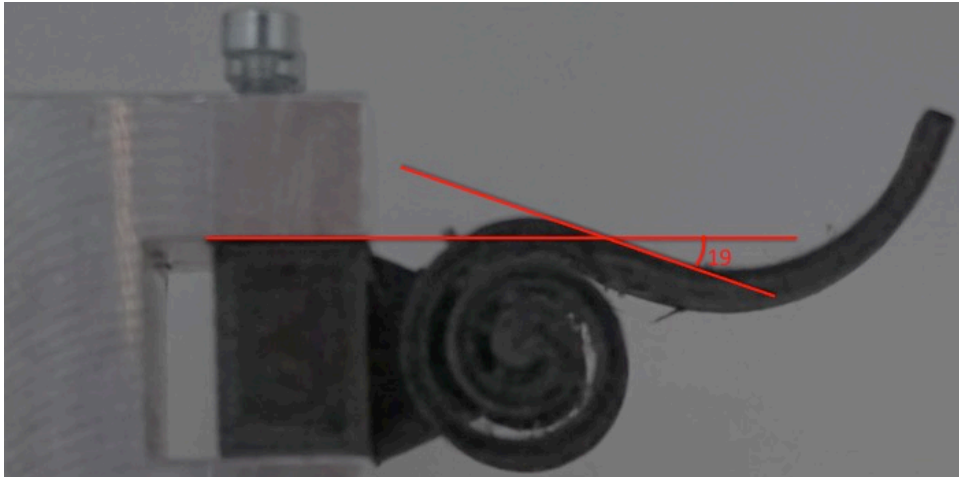


Figure 67. The front view of the second spiral sample, after fatigue testing, being held in the clamping stand. The sample was unable to return to its original position by an angle of nineteen degrees.